

# Adding geometry to fingerprinting localization with Euclidean Distance Matrix (EDM)

Robin Solignac

Master Thesis  
Systems of Communication  
Submitted 15 march 2019  
École Polytechnique Fédérale de Lausanne, IC faculty

LCAV  
Swisscom Digital Lab

Supervisors:  
Adam Scholefield, LCAV  
Guillermo Barrenetxea, Swisscom

Lausanne, EPFL, 2019





# Acknowledgements

Lorem ipsum dolor sit amet, consectetuer adipiscing elit. Ut purus elit, vestibulum ut, placerat ac, adipiscing vitae, felis. Curabitur dictum gravida mauris. Nam arcu libero, nonummy eget, consectetuer id, vulputate a, magna. Donec vehicula augue eu neque. Pellentesque habitant morbi tristique senectus et netus et malesuada fames ac turpis egestas. Mauris ut leo. Cras viverra metus rhoncus sem. Nulla et lectus vestibulum urna fringilla ultrices. Phasellus eu tellus sit amet tortor gravida placerat. Integer sapien est, iaculis in, pretium quis, viverra ac, nunc. Praesent eget sem vel leo ultrices bibendum. Aenean faucibus. Morbi dolor nulla, malesuada eu, pulvinar at, mollis ac, nulla. Curabitur auctor semper nulla. Donec varius orci eget risus. Duis nibh mi, congue eu, accumsan eleifend, sagittis quis, diam. Duis eget orci sit amet orci dignissim rutrum.

Nam dui ligula, fringilla a, euismod sodales, sollicitudin vel, wisi. Morbi auctor lorem non justo. Nam lacus libero, pretium at, lobortis vitae, ultricies et, tellus. Donec aliquet, tortor sed accumsan bibendum, erat ligula aliquet magna, vitae ornare odio metus a mi. Morbi ac orci et nisl hendrerit mollis. Suspendisse ut massa. Cras nec ante. Pellentesque a nulla. Cum sociis natoque penatibus et magnis dis parturient montes, nascetur ridiculus mus. Aliquam tincidunt urna. Nulla ullamcorper vestibulum turpis. Pellentesque cursus luctus mauris.

*Lausanne, 12 Mars 2011*

D. K.



# **Abstract**

Lore ipsum dolor sit amet, consectetuer adipiscing elit. Ut purus elit, vestibulum ut, placerat ac, adipiscing vitae, felis. Curabitur dictum gravida mauris. Nam arcu libero, nonummy eget, consectetuer id, vulputate a, magna. Donec vehicula augue eu neque. Pellentesque habitant morbi tristique senectus et netus et malesuada fames ac turpis egestas. Mauris ut leo. Cras viverra metus rhoncus sem. Nulla et lectus vestibulum urna fringilla ultrices. Phasellus eu tellus sit amet tortor gravida placerat. Integer sapien est, iaculis in, pretium quis, viverra ac, nunc. Praesent eget sem vel leo ultrices bibendum. Aenean faucibus. Morbi dolor nulla, malesuada eu, pulvinar at, mollis ac, nulla. Curabitur auctor semper nulla. Donec varius orci eget risus. Duis nibh mi, congue eu, accumsan eleifend, sagittis quis, diam. Duis eget orci sit amet orci dignissim rutrum.

Nam dui ligula, fringilla a, euismod sodales, sollicitudin vel, wisi. Morbi auctor lorem non justo. Nam lacus libero, pretium at, lobortis vitae, ultricies et, tellus. Donec aliquet, tortor sed accumsan bibendum, erat ligula aliquet magna, vitae ornare odio metus a mi. Morbi ac orci et nisl hendrerit mollis. Suspendisse ut massa. Cras nec ante. Pellentesque a nulla. Cum sociis natoque penatibus et magnis dis parturient montes, nascetur ridiculus mus. Aliquam tincidunt urna. Nulla ullamcorper vestibulum turpis. Pellentesque cursus luctus mauris.

Key words:



# Contents

<b>Acknowledgements</b>	<b>i</b>
<b>Abstract</b>	<b>iii</b>
<b>List of figures</b>	<b>vii</b>
<b>List of tables</b>	<b>ix</b>
<b>1 Introduction</b>	<b>1</b>
1.1 Introduction . . . . .	1
1.2 Objective and scope . . . . .	2
1.3 Thesis organization . . . . .	3
<b>2 Failure criteria</b>	<b>5</b>
2.1 Introduction . . . . .	5
2.2 Review . . . . .	7
2.2.1 Mohr-Coulomb criterion . . . . .	7
2.2.2 Hoek-Brown criterion . . . . .	12
2.2.3 Paul-Mohr-Coulomb criterion . . . . .	14
2.3 Paul-Mohr-Coulomb fitting . . . . .	18
<b>3 Dunnville sandstone</b>	<b>21</b>
3.1 Geology, mineralogy and properties of the Dunnville sandstone . . . . .	21
3.1.1 Geological history . . . . .	21
3.1.2 Mineralogy . . . . .	21
3.2 Uniaxial compression test . . . . .	23
3.2.1 Specimen preparation . . . . .	23
3.2.2 Procedure . . . . .	23
3.2.3 Results . . . . .	23
3.3 Conventional triaxial tests . . . . .	24
3.3.1 Hoek-Franklin cell . . . . .	25
3.3.2 Specimen preparation . . . . .	26
3.3.3 Conventional triaxial compression test . . . . .	27
3.3.4 Conventional triaxial compression test . . . . .	28
3.3.5 Results . . . . .	29

## Contents

---

<b>4 Multi-axial experiments</b>	<b>37</b>
4.1 Introduction . . . . .	37
4.2 Multi-axial apparatus . . . . .	38
4.2.1 Development of the apparatus . . . . .	38
4.2.2 Description of the apparatus . . . . .	38
4.3 Specimen preparation . . . . .	40
4.3.1 Dimensions . . . . .	40
4.3.2 Specimen instrumentation . . . . .	40
4.3.3 Jacketing . . . . .	42
4.4 Experiments . . . . .	43
4.4.1 True-triaxial testing . . . . .	44
4.4.2 Axisymmetric triaxial compression experiment on a prismatic specimen	47
4.5 Results . . . . .	50
4.5.1 True-triaxial experiment under plane strain condition . . . . .	50
4.5.2 Axisymmetric triaxial compression experiment on a prismatic specimen	51
4.5.3 True-triaxial experiment under constant mean stress condition . . . . .	53
<b>5 Results analysis and Discussion</b>	<b>57</b>
5.1 Overview . . . . .	57
5.2 Evaluation of the failure criteria . . . . .	57
5.2.1 Mohr-Coulomb failure criterion . . . . .	59
5.2.2 Hoek-Brown failure criterion . . . . .	60
5.2.3 Paul-Mohr-Coulomb failure criterion with one plane . . . . .	62
5.2.4 Comparison of the failure criteria . . . . .	67
5.3 Paul-Mohr-Coulomb failure criterion with two planes . . . . .	68
5.3.1 Paul-Mohr-Coulomb with six parameters . . . . .	68
5.3.2 2-planes fitting . . . . .	69
5.3.3 Dunnville sandstone . . . . .	72
5.4 Discussion . . . . .	78
<b>6 Conclusion</b>	<b>81</b>
6.1 Conclusion . . . . .	81
6.2 Future work . . . . .	82
<b>Bibliography</b>	<b>84</b>

# List of Figures

2.1 Failure surface in (a) the principal stress space and (b) the $\pi$ -plane [1, Labuz 2018]	7
2.2 Mohr-Coulomb criterion failure surface in $(\sigma_3 - \sigma_1)$ plane . . . . .	9
2.3 Schematic representation of Mohr-Coulomb criterion failure surface in $(p - s)$ plane	11
2.4 Schematic representation of Mohr-Coulomb criterion failure surface in $\pi$ plane	12
2.5 Schematic representation of Hoek-Brown criterion failure surface in $(\sigma_3 - \sigma_1)$ plane. . . . .	14
2.6 Schematic representation of Hoek-Brown criterion failure surface in $(p - q)$ plane.	15
2.7 Schematic representation of Hoek-Brown criterion failure surface in $\pi$ plane. . . . .	16
2.8 Schematic representation of Paul-Mohr-Coulomb criterion failure surface in $(\sigma_3 - \sigma_1)$ plane. . . . .	17
3.1 Dunnville sandstone mineralogy . . . . .	22
3.2 Stress and Strain relationship for the uniaxial compression test . . . . .	25
3.3 Stress and Strain relationship for the uniaxial compression test . . . . .	26
3.4 Hoek-Franklin cell . . . . .	27
3.5 Conventional triaxial test set up . . . . .	28
3.6 Membrane hosting the rock specimen in the Hoek-Franklin cell . . . . .	29
3.7 Strain Gage set up on a CTC specimen . . . . .	30
3.8 Summary of the stress-strain relationships for the triaxial compression and extension tests . . . . .	32
3.9 Mohr-Coulomb circles for the conventional triaxial compression tests. . . . .	34
3.10 Poisson's ratio of Dunnville sandstone . . . . .	34
3.11 Theoretical specimen failure . . . . .	35
4.1 Base unit of the Plane-Strain Apparatus . . . . .	39
4.2 Biaxial Frame of the Plane-Strain Apparatus . . . . .	39
4.3 Loading piston of the Plane-Strain Apparatus . . . . .	41
4.4 Pressure cell of the Plane-Strain Apparatus . . . . .	41
4.5 a. Specimen dimensions and b. loading directions . . . . .	42
4.6 Specimen instrumented with axial and transversal strain gages . . . . .	42
4.7 a) Jacketed specimen and b) coating set-up . . . . .	43
4.8 Apparatus set-up for the true-triaxial experiments . . . . .	45
4.9 Apparatus set-up for the axisymmetric triaxial experiment on a prismatic specimen	48

## List of Figures

---

4.10 $\sigma - \epsilon_a$ plot for the true-triaxial experiment performed under plane strain condition . . . . .	51
4.11 $\epsilon$ - time plot for true-triaxial experiment under plane strain condition . . . . .	52
4.12 Failure surface of the TT 1 specimen . . . . .	53
4.13 $\sigma - \epsilon_a$ plot for the axisymmetric triaxial compression experiment . . . . .	54
4.14 Failure surface of the TT2 specimen from the side and bottom . . . . .	55
4.15 Sketch of the procedure for true-triaxial experiment under constant mean stress condition . . . . .	56
4.16 Failure surface on constant mean stress test specimen . . . . .	56
5.1 Mohr-Coulomb criterion failure surface in $(\sigma_3 - \sigma_1)$ plane . . . . .	61
5.2 Mohr-Coulomb criterion failure surface in $(p - q)$ plane . . . . .	61
5.3 Mohr-Coulomb criterion failure surface in $\pi$ -plane . . . . .	62
5.4 Hoek-Brown criterion failure surface in $(\sigma_3 - \sigma_1)$ plane . . . . .	63
5.5 Hoek-Brown criterion failure surface in $(p - q)$ plane . . . . .	63
5.6 Hoek-Brown criterion failure surface in $\pi$ -plane . . . . .	64
5.7 Paul-Mohr-Coulomb criterion failure surface in $(\sigma_3 - \sigma_1)$ plane . . . . .	66
5.8 Paul-Mohr-Coulomb criterion failure surface in $(p - q)$ plane . . . . .	66
5.9 Paul-Mohr-Coulomb criterion failure surface in $\pi$ -plane . . . . .	67
5.10 Paul-Mohr-Coulomb 6-12-6 sided failure surface graphical representations . . . . .	70
5.11 Paul-Mohr-Coulomb 6-12-6 sided failure surface in $(\sigma_{II} - \sigma_I)$ plane . . . . .	71
5.12 Paul-Mohr-Coulomb failure surface in the $(p - q)$ plane for Dunnville sandstone . . . . .	75
5.13 Paul-Mohr-Coulomb failure surface in the $(\sigma_{II} - \sigma_I)$ plane for Dunnville sandstone . . . . .	75
5.14 Paul-Mohr-Coulomb failure surface in the $\pi$ -plane for Dunnville sandstone . . . . .	76
5.15 6-12-6 sided pyramid projection in the $\pi$ -plane for Dunnville sandstone . . . . .	76
5.16 Paul-Mohr-Coulomb 6-12-6 sided failure surface pyramid for Dunnville sandstone . . . . .	77

# List of Tables

3.1	Mineralogy of Dunnville Sandstone [2] . . . . .	22
3.2	Summary of CTC and CTE tests results . . . . .	31
3.3	Mohr-Coulomb strength parameters for various stress regimes for Dunnville sandstone . . . . .	31
3.4	Failure surfaces for conventional triaxial compression tests . . . . .	33
3.5	Failure surfaces for conventional triaxial extension tests . . . . .	33
4.1	Results of the true-triaxial experiment under plane-strain condition . . . . .	50
4.2	Results of the axisymmetric triaxial experiment on a prismatic specimen . . . . .	51
4.3	Results of the true-triaxial experiment under plane-strain condition . . . . .	52
4.4	Results of the true-triaxial experiment under plane-strain condition . . . . .	55
5.1	Database of experiments results for Dunnville Sandstone. The "Published" data are from Zeng et al. (2019) [3] . . . . .	58
5.2	Summary of the mean standard deviation misfits obtained for the three failure criteria evaluated . . . . .	68
5.3	Parameters of the planes defining the failure surface of Paul-Mohr-Coulomb criterion . . . . .	69
5.4	Types of failure surfaces for the six parameters Paul-Mohr-Coulomb criterion .	69
5.5	$P_1$ and $P_2$ least-square solutions $x$ for Dunnville sandstone . . . . .	74
5.6	$P_1$ and $P_2$ strength parameters for Dunnville sandstone . . . . .	74
5.7	$P_1$ and $P_2$ fitting parameters for Dunnville sandstone . . . . .	74
5.8	Paul-Mohr-Coulomb general equation coefficients for Dunnville sandstone .	74
5.9	Summary of $P_1$ and $P_2$ strength parameters for Dunnville sandstone . . . . .	74



# 1 Introduction

## 1.1 Introduction

The wide variety of rocks that forms the earth crust makes constitutive modeling a challenge. In some sense, each formation can in itself be considered as a different material, with diverse mineralogy, geological history and behavior. However, a common thread is their composite structure formed by solids (minerals), pores, and cracks [1]. Years of research on these materials show similarities in results, through the definition of material parameters used to characterize their behavior. Analysis and interpretation of these experimental outcomes are key elements in the understanding of rock response, and enables safer prediction of their behavior, which is used in the design of geotechnical structures.

Rock response under a certain state of stress is often characterized by its strength. Multiple experiments, such as axisymmetric triaxial and multi axial tests, have been developed with the aim of getting information on the various states of stress that lead to failure. However, site-specific rock engineering properties are often not available during the preliminary design phase of structures constructed on or into the rock mass. Therefore, models are widely used in the initial stage of the design for prediction of the engineering properties of the rock mass.

Over the last century, many predictive models have been developed for failure. These models describe surfaces in  $(\sigma_1-\sigma_2-\sigma_3)$  space that approximate experimental data, where  $\sigma_1$ ,  $\sigma_2$  and  $\sigma_3$  are principal stresses with no regard to order. The plethora of failure criteria arise from the challenge of finding one that can give the most accurate description of rock behavior. Empirical models are usually developed for a specific rock type or rock formation and therefore, need to be evaluated before they can be applied to a design.

The most well-known and widely used failure criterion is the Mohr-Coulomb (MC) model, which provides a linear relationship between the normal stress and shear stress on the failure plane. The slope of the failure envelope is characterized by the friction angle  $\phi$  and the shear-stress intercept, also called cohesion  $c$  [4]. MC can also be written in terms of principal stresses  $\sigma_I$  and  $\sigma_{III}$ , respectively the major and minor principal stresses; note that the intermediate

stress  $\sigma_{II}$  does not appear. Other criterion, such as the Hoek-Brown (HB) model for intact rocks and rock masses, are non-linear in the Mohr and  $(\sigma_{III} - \sigma_I)$  plane [5]. HB provides a reasonable estimate of the state of stress at failure, especially for low values confining stress, minor principal stress  $\sigma_{III} < C_0/3$  the uniaxial compressive strength. These failure criteria may be written in terms of the major ( $\sigma_1$ ) and minor ( $\sigma_3$ ) principal stresses, without any consideration to effect of intermediate principal stress ( $\sigma_2$ ).

Experiments, have shown that the intermediate principal stress affects the mode of failure and the principal stresses that are developed at failure [1, 6, 3, 7]. Moreover, the failure envelope that describe best the experimental data is not linear over a large range of mean stress.

To address the limitations of the  $\sigma_I - \sigma_{III}$  failure criteria such as that of Mohr-Coulomb, and following the pioneering work of Paul (1968), other investigators, developed a failure criterion that accounts for the three principal stresses,  $\sigma_I$ ,  $\sigma_{II}$  and  $\sigma_{III}$  [8, 9]. The piecewise linear failure surface enables a more accurate prediction of the rock behavior, especially at high mean stress.

This new approach to represent rock failure and the corresponding stress state requires material constants to be evaluated and calibrated using multi axial strength tests. Experimentation is the key element in the quest evaluating failure criteria. In order to be recognized as accurate, the criterion should provide a failure surface that gives good prediction of the test results. It is also important that the chosen experiments are diverse and representative of the state of stress in the field. Indeed, a failure criterion well suited for the prediction of a particular test could lead to a poor estimate for another test. Therefore, additional test data will help to provide a more accurate evaluation of the model parameters for the failure criterion proposed by Paul (1968) and forms the impetus for the present work [8].

## 1.2 Objective and scope

The main objective of the work presented in this thesis is to explore the nature of stress states at failure as described by the three principal stresses and to investigate the accuracy of three failure criteria. A laboratory testing program was devised to study the mechanical properties of the Dunnville sandstone, to evaluate the existing failure criteria and to calibrate the Paul-Mohr-Coulomb model for this rock. The following define the scope of this thesis:

1. Laboratory tests including uniaxial compression, axisymmetric (triaxial) compression and extension tests are performed to characterize the elastic parameters such as Young's modulus ( $E$ ) and Poisson's ratio ( $\nu$ ), and failure parameters such as friction angle in compression and extension ( $\phi_c$  and  $\phi_e$ , respectively).
2. Many geo-engineering problems involves rock subjected to a plane state of strain. It is particularly the case for tunnels, and other long structures with a constant cross-section and loaded in the plane of the cross-section [4]. A true-triaxial device is used to simulate

a plane strain condition, where the minor principal stress ( $\sigma_{III}$ ) is maintained at a desired target value and the intermediate stress ( $\sigma_{II}$ ) is increased to develop a condition where  $\Delta_{\epsilon_2} = 0$  is simulated.

3. A true triaxial device is used to develop a stress path to failure where the mean stress is kept constant during the deviatoric loading stage by decreasing the intermediate principal stress ( $\sigma_2$ ) as failure is approached.
4. The test results from this thesis and those reported in literature used to evaluate various failure criteria, including the model parameters for the Paul-Mohr-Coulomb (general linear) failure criterion.

### **1.3 Thesis organization**

Chapter 2 presents a review of three widely used failure criteria namely, Mohr-Coulomb, Hoek-Brown and Paul-Mohr-Coulomb. Chapter 3 summarizes the geologic history and mineralogy of Dunnville sandstone as well as the results of uniaxial and conventional triaxial (compression and extension) tests on samples of Dunnville sandstone. Chapter 4 reviews the theoretical background on true triaxial experiments performed in this study, and the results of plane strain and constant mean stress tests are presented. In Chapter 5, the new test data and the existing data from published literature are used to (i) evaluate existing failure criteria, and (ii) calibrate the Paul-Mohr-Coulomb failure criterion. Chapter 6 presents the conclusions and important findings of this thesis.

The symbols and notations used in this thesis are listed in APPENDIX A REFAPPENDIX A.



## 2 Failure criteria

Failure criteria aim to describe in the most accurate way rock failure under various states of stress. The most successful criteria are usually a generalization of experimental results, from a combination of axisymmetric and multi-axial tests. Indeed, failure criteria are a theoretical conjecture aimed to describe what is observed from material behavior. In this chapter, a presentation of the mathematical formulation of selected criteria is reviewed.

### 2.1 Introduction

Many investigators have attempted to develop models or mathematical expression to describe the failure of rock [1]. These criteria are usually of an empirical nature and stress based:

$$f(\sigma_{xx}, \sigma_{yy}, \sigma_{zz}, \sigma_{xy}, \sigma_{yz}, \sigma_{zx}) = \text{constant} \quad (2.1)$$

Equation 2.1 can be simplified in the case of isotropic materials and the six-parameters stress space can be reduced to three. Indeed, isotropic rock possesses strength properties that are the same in all directions, leading to directional independence. Therefore, the function can then be written in terms of principal stresses:

$$f(\sigma_I, \sigma_{II}, \sigma_{III}) = \text{constant} \quad (2.2)$$

where  $\sigma_I$ ,  $\sigma_{II}$  and  $\sigma_{III}$  are the major, intermediate and minor principal stresses. In addition, other stress invariants can be used:

$$f(I_I, J_{II}, J_{III}) = \text{constant} \quad (2.3)$$

$I_I$  is the first invariant of the stress tensor  $\sigma_{ij}$ ,  $J_{II}$  and  $J_{III}$  are respectively, the second and

third invariants of the deviatoric stress tensor  $S_{ij} = \sigma_{ij} - p\delta_{ij}$ :

$$I_1 = \sigma_I + \sigma_{II} + \sigma_{III} \quad (2.4)$$

$$J_2 = \frac{1}{6} [(\sigma_I - \sigma_{II})^2 + (\sigma_{II} - \sigma_{III})^2 + (\sigma_{III} - \sigma_I)^2] \quad (2.5)$$

$$J_3 = (\sigma_I - p)(\sigma_{II} - p)(\sigma_{III} - p) \quad (2.6)$$

Three others can be defined, and will be used in this thesis: the mean stress  $p$ , the deviatoric stress  $q$  and the Lode angle  $\theta$ :

$$f(p, q, \theta) = \text{constant} \quad (2.7)$$

with

$$p = \frac{I_1}{3} = \frac{\sigma_I + \sigma_{II} + \sigma_{III}}{3} \quad (2.8)$$

$$q = \sqrt{3J_2} = \frac{1}{6}\sqrt{[(\sigma_I - \sigma_{II})^2 + (\sigma_{II} - \sigma_{III})^2 + (\sigma_{III} - \sigma_I)^2]} \quad (2.9)$$

$$\theta = \frac{1}{3} \arccos \left( \frac{3\sqrt{3}}{2} \frac{J_3}{J_2^{3/2}} \right) = \arctan \left[ \frac{\sqrt{3}(\sigma_M - \sigma_m)}{2\sigma_I - \sigma_{II} - \sigma_{III}} \right] \quad (2.10)$$

The Lode angle is a measure of the stress state:  $0^\circ \leq \theta \leq 60^\circ$ , particularly  $\theta = 0^\circ$  for axisymmetric compression  $\sigma_{II} = \sigma_{III}$  and  $\theta = 60^\circ$  in the case of axisymmetric extension ( $\sigma_{II} = \sigma_I$ ).

Equations 2.2, 2.3 and 2.7 suggest that the failure surface and consequently the failure criterion has a three-dimensional nature. Indeed, depending on the stress ordering, failure criteria describe six surfaces in a three-dimensional  $\sigma_1 - \sigma_2 - \sigma_3$  space: (i)  $\sigma_1 \geq \sigma_2 \geq \sigma_3$ , (ii)  $\sigma_2 \geq \sigma_1 \geq \sigma_3$ , (iii)  $\sigma_2 \geq \sigma_3 \geq \sigma_1$ , (iv)  $\sigma_3 \geq \sigma_2 \geq \sigma_1$ , (v)  $\sigma_3 \geq \sigma_1 \geq \sigma_2$ , (vi)  $\sigma_1 \geq \sigma_3 \geq \sigma_1$ . For example, a linear criterion, written in terms of the three principal stresses,  $\sigma_I$ ,  $\sigma_{II}$ ,  $\sigma_{III}$ , shows a pyramidal shape where the planes have a common vertex  $V_0$  (the theoretical isotropic tensile strength), which is located on the tension side of the space (see Figure 2.1a).

Although the three-dimensional representation of the failure surface is the most complete, other views are often used. For example, two-dimensional coordinate systems such as  $(\sigma_3 - \sigma_1)$ ,  $(p - q)$  plane and the  $\pi$ -plane are simple to view.

The  $\pi$ -plane. is a section of the failure surface in the principal stress space, perpendicular to the hydrostatic axis. It is also called the equipressure plane, as the mean stress is constant over the plane. Moreover, the axes  $(\sigma_1^*, \sigma_2^*, \sigma_3^*)$  are the projection of the coordinate axis on the

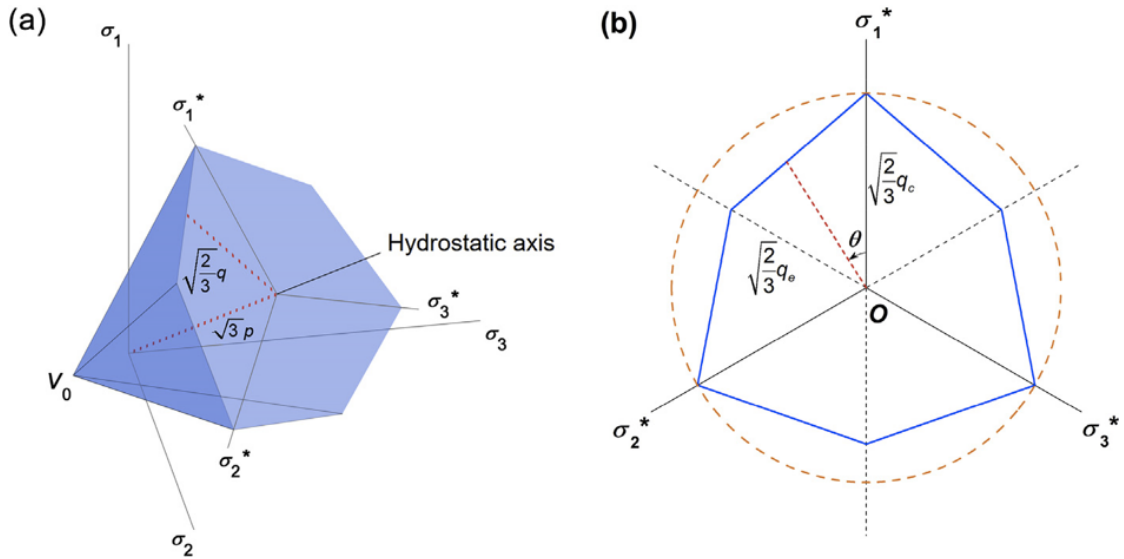


Figure 2.1: Failure surface in (a) the principal stress space and (b) the  $\pi$ -plane [1, Labuz 2018]

$\pi$ -plane (cf. 2.1b.). Each point in principal stress space can be represented in polar coordinates in this plane. As the mean stress is constant over the  $\pi$ -plane, the point is at a distance  $r$  from the origin of the hydrostatic axis and oriented at the Lodge angle  $\theta$  from the  $\sigma_1^*$  axis. Then the principal coordinates of the same point on the  $\pi$ -plane can be written as:

$$\sigma_1 = p + \frac{\sqrt{6}}{3}r \cos(\theta) \quad (2.11)$$

$$\sigma_2 = p - \frac{\sqrt{6}}{3}r \sin\left(\frac{\pi}{6} - \theta\right) \quad (2.12)$$

$$\sigma_3 = p - \frac{\sqrt{6}}{3}r \sin\left(\frac{\pi}{6} + \theta\right) \quad (2.13)$$

In the next sections, selected failure criteria will be presented along with their formulation in each coordinates system.

## 2.2 Review

### 2.2.1 Mohr-Coulomb criterion

The Mohr-Coulomb failure criterion (MC) is the most popular and widely used criterion. It provides a relationship between the shear stress and normal stress  $\sigma$  acting on the failure plane. The failure envelope may be represented using two material parameters known as the

internal failure angle  $\phi$  and the cohesion  $c$ :

$$\tau = \sigma \tan \phi + c \quad (2.14)$$

The Mohr-Coulomb failure criterion does not consider the effect of the intermediate principal stress. The shear and normal stresses may be written in terms of the major and minor principal stresses:

$$\tau = \frac{\sigma_I - \sigma_{III}}{2} \cos \phi \quad (2.15)$$

$$\sigma = \frac{\sigma_I + \sigma_{III}}{2} - \frac{\sigma_I - \sigma_{III}}{2} \sin \phi \quad (2.16)$$

Substitution of Equations 2.15 and 2.16 in Equation 2.14 leads to a form of the Mohr-Coulomb failure criterion in terms of the major and minor principal stresses:

$$\sigma_I = \frac{1 + \sin \phi}{1 - \sin \phi} \sigma_{III} + \frac{2c \cos \phi}{1 - \sin \phi} \quad (2.17)$$

or alternatively

$$\sigma_I = K_p \sigma_{III} + C_0 \quad (2.18)$$

where  $K_p$  is the slope of the failure surface in  $(\sigma_3 - \sigma_1)$  plane and  $C_0$  is the uniaxial compression strength of the rock.

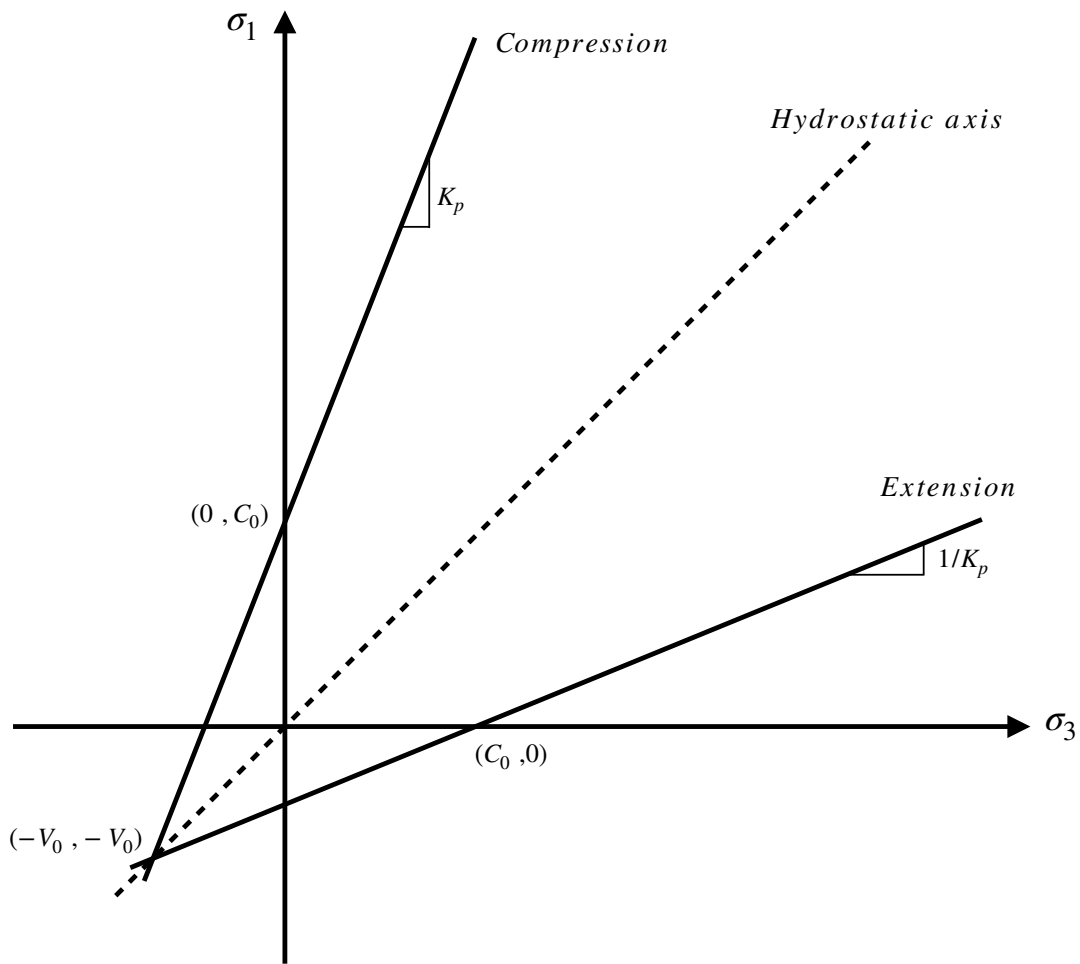
### Mohr-Coulomb in the $(\sigma_3 - \sigma_1)$ plane

Fig 2.2 presents the graphical construction of Mohr-Coulomb envelope in the  $(\sigma_3 - \sigma_1)$  plane. The common vertex of the failure surfaces in extension and compression can be expressed using  $\sigma_I = \sigma_{III} = -V_0$ :

$$V_0 = \frac{C_0}{K_p - 1} \quad (2.19)$$

As Mohr-Coulomb does not consider the intermediate stress effect, it may be conveniently used to represent the failure for rocks subjected to stress states that may be replicated in axisymmetric triaxial tests.

Conventional (axisymmetric) Triaxial Compression (CTC):


 Figure 2.2: Mohr-Coulomb criterion failure surface in  $(\sigma_3 - \sigma_1)$  plane

$$\sigma_I = \sigma_a \quad (2.20)$$

$$\sigma_{III} = \sigma_r \quad (2.21)$$

$$\sigma_{II} = \sigma_{III} = \sigma_r \quad (2.22)$$

Conventional (axisymmetric) Triaxial Extension (CTE):

$$\sigma_I = \sigma_r \quad (2.23)$$

$$\sigma_{III} = \sigma_a \quad (2.24)$$

$$\sigma_{II} = \sigma_I = \sigma_r \quad (2.25)$$

**Mohr-Coulomb in the  $(p - q)$  plane**

The Mohr-Coulomb model can also be represented in  $(p - q)$  plane. For example, in axisymmetric triaxial compression, Equations 2.8 and 2.9 can be written as:

$$p = \frac{\sigma_a + 2\sigma_r}{2} \quad (2.26)$$

$$q = \sigma_a - \sigma_r \quad (2.27)$$

By rearranging Equation 2.17 and incorporating the conditions for CTC, Mohr-Coulomb criterion becomes:

$$(\sigma_a - \sigma_r) = (\sigma_a + \sigma_r) \sin \phi + 2c \cos \phi \quad (2.28)$$

Expanding and substituting Equation 2.26 and 2.26 into 2.28, the following equation is obtained::

$$q(3 - \sin \phi) = 6p \sin \phi + 6c \cos \phi \quad (2.29)$$

Finally, the Mohr-Coulomb failure surface formulation in the  $(p - q)$  plane is defined by Equation 2.30 for CTC:

$$q = \frac{6 \sin \phi}{3 - \sin \phi} p + \frac{6c \cos \phi}{3 - \sin \phi} \quad (2.30)$$

Following the same approach as that for CTC, the M-C criterion for CTE may be written as:

$$q = \frac{6 \sin \phi}{3 + \sin \phi} p + \frac{6c \cos \phi}{3 + \sin \phi} \quad (2.31)$$

or in the condensed form:

$$q = m_{c,e} p + b_{c,e} \quad (2.32)$$

where  $c$  and  $e$  defines  $m$  and  $b$  for compression or extension surfaces:

$$m_c = \frac{6 \sin \phi}{3 - \sin \phi} \quad (2.33)$$

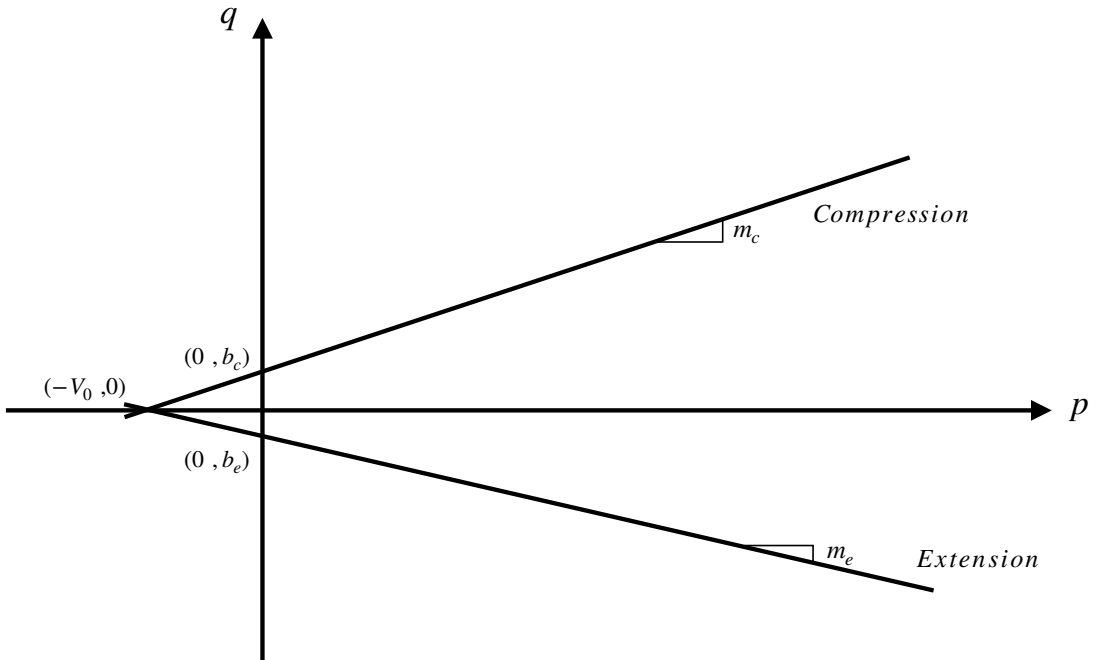


Figure 2.3: Schematic representation of Mohr-Coulomb criterion failure surface in  $(p - s)$  plane

$$m_e = \frac{6 \sin \phi}{3 + \sin \phi} \quad (2.34)$$

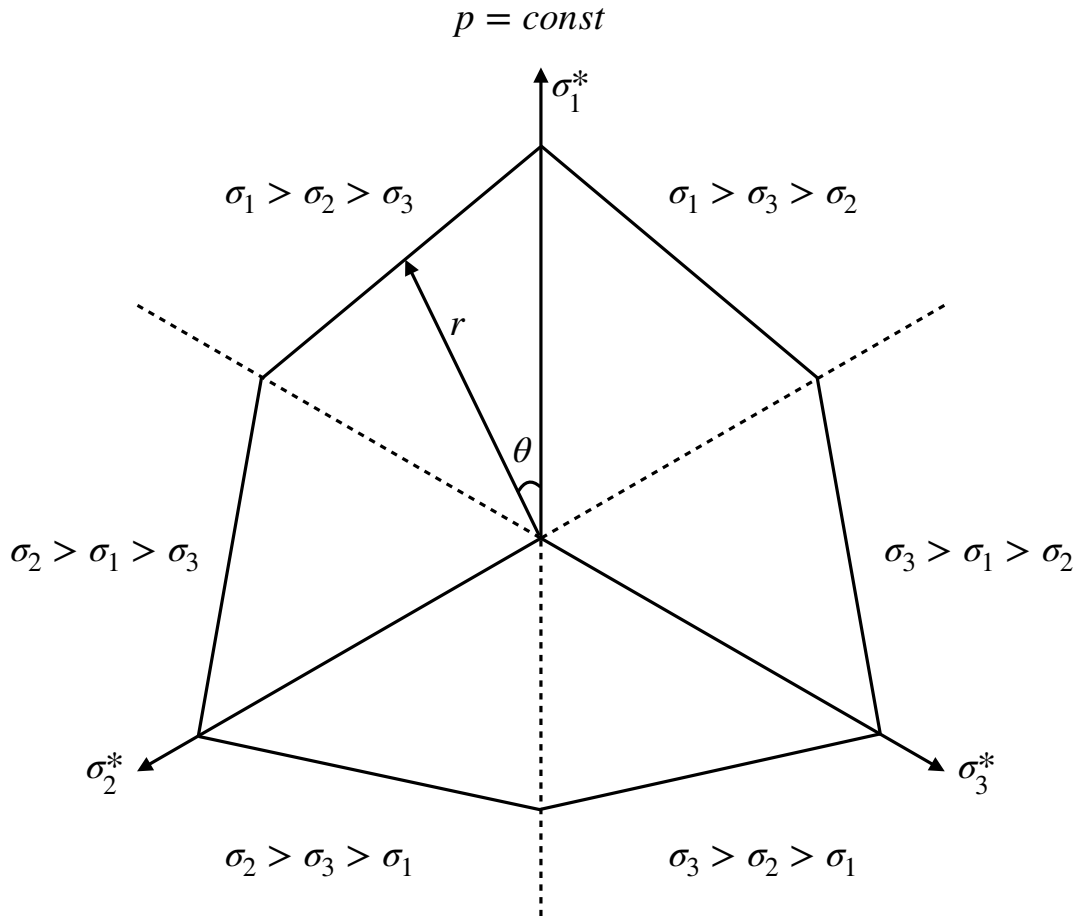
$$b_c = \frac{6c \cos \phi}{3 - \sin \phi} \quad (2.35)$$

$$b_e = \frac{6c \cos \phi}{3 + \sin \phi} \quad (2.36)$$

Figure 2.3 presents the graphical construction of the failure surfaces in the  $(p - q)$  plane. In order to distinguish compression from extension data, the failure surface in extension is shown using a negative deviatoric stress  $-q$ .

### Mohr-Coulomb in the $\pi$ -plane

The Mohr-Coulomb failure envelope in the  $\pi$ -plane is presented in Figure 2.4. The failure surfaces can be obtained by inserting Equation 2.11 and 2.13 in the criterion formulation defined by 2.18. The obtained expressions and their development are presented in APPENDIX B REFAPPENDIX B.


 Figure 2.4: Schematic representation of Mohr-Coulomb criterion failure surface in  $\pi$  plane

### 2.2.2 Hoek-Brown criterion

The Hoek-Brown (HB) criterion is a non-linear model for isotropic rocks that does not account for the intermediate principal stress. The criterion may be written as:

$$\sigma_I = \sigma_{III} + C_0 \sqrt{m \frac{\sigma_{III}}{C_0} + s} \quad (2.37)$$

Hoek and Brown (1980) [5] define  $m$  and  $s$  as constants that depends on the rock type and “blockiness”. The constant  $s$  characterizes the initial state of the tested rock. For intact rock,  $s = 1.0$  and the strength parameter  $m$  is an empirical fitting parameter chosen depending on the rock type.

### Hoek-Brown in the $(\sigma_3 - \sigma_1)$ plane

In  $(\sigma_3 - \sigma_1)$  coordinate system, and for the axisymmetric triaxial compression tests, the Hoek-Brown criterion may be written as:

$$\sigma_a = \sigma_r + C_0 \sqrt{m \frac{\sigma_r}{C_0} + 1} \quad (2.38)$$

Similarly, the formulation for axisymmetric triaxial extension is written as:

$$\sigma_a = \sigma_r - \frac{\sqrt{4mC_0\sigma_r + m^2C_0^2 + 4C_0^2 - mC_0}}{2} \quad (2.39)$$

From Equation 2.38, the theoretical isotropic tensile strength  $V_0$  can be expressed as a function of the uniaxial compression strength  $C_0$ , using :  $\sigma_a = \sigma_r = -V_0$ :

$$V_0 = \frac{C_0}{m} \quad (2.40)$$

Figure 2.5 presents the Hoek-Brown failure surfaces in the  $(\sigma_3 - \sigma_1)$  coordinates system.

### Hoek-Brown in the $(p - q)$ plane

Hoek-Brown criterion may also be expressed with the stress invariants  $p$  and  $q$ . By rearranging Equation 2.37 the formulation becomes:

$$(\sigma_I - \sigma_{III})^2 = C_0^2 \left( m \frac{\sigma_{III}}{C_0} + s \right) \quad (2.41)$$

By rearranging and inserting  $p$  and  $q$  in Equation 2.41, implicit formulation for CTC and CTE are obtained. Equation 2.42 for compression and 2.43 for extension describe Hoek-Brown criterion after solving roots of the implicit expressions:

$$q = \frac{1}{6} \left( \pm \sqrt{C_0} \sqrt{C_0 m^2 + 36C_0 + 36mp} - C_0 m \right) \quad (2.42)$$

$$q = \frac{1}{3} \left( \pm \sqrt{C_0^2 m^2 + 9C_0^2 + 9C_0 mp} + C_0 m \right) \quad (2.43)$$

The Hoek-Brown criterion surface fitting in the  $(p - q)$  plane is presented in Figure 2.6, where the positive root of Equation 2.42 and the negative root of Equation 2.43 are considered.

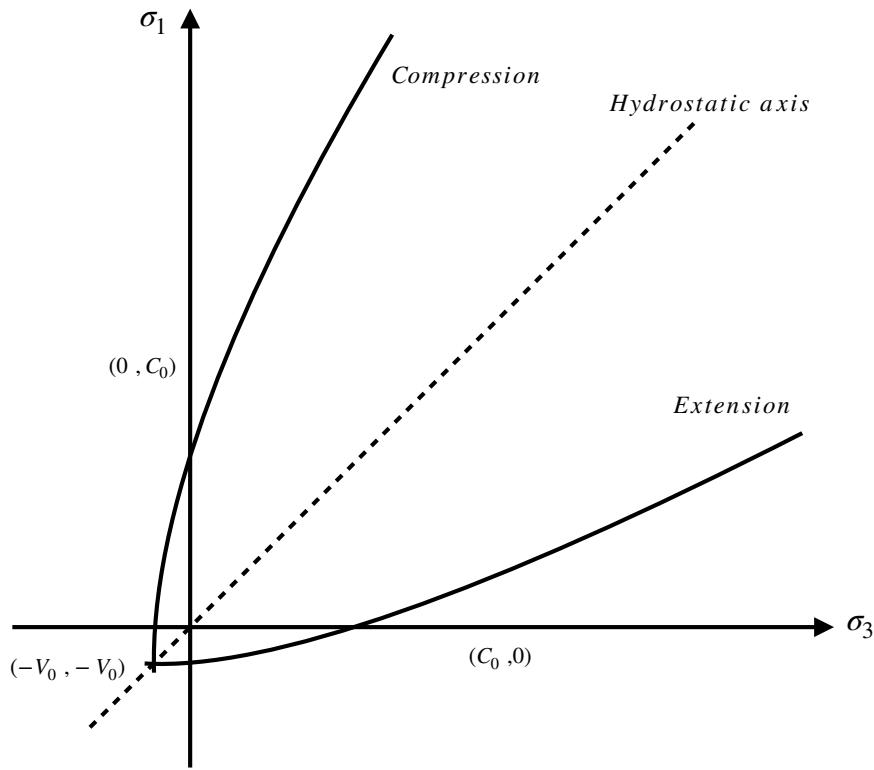


Figure 2.5: Schematic representation of Hoek-Brown criterion failure surface in  $(\sigma_3 - \sigma_1)$  plane.

### Hoek-Brown in the $\pi$ plane

The Hoek-Brown failure criterion in the  $\pi$ -plane is presented in Figure 2.7. The failure surfaces can be obtained by inserting Equation 2.11 and 2.13 in 2.37. The obtained expressions and their development are presented in APPENDIX B REFAPPENDIX B. In Figure 2.7, the surfaces are exaggerated to show the non-linearity of the criterion.

### 2.2.3 Paul-Mohr-Coulomb criterion

The Paul-Mohr-Coulomb criterion (PMC) is a linear model in terms of the three principal stresses. Unlike Mohr-Coulomb and Hoek-Brown, the Paul-Mohr-Coulomb criterion may be used to represent the effect of all principal stresses on rock behavior at failure. Its formulation is based on the one developed by Mohr-Coulomb, for which the intermediate stress effect is added [8]. The Paul-Mohr-Coulomb failure criterion have the following general expression:

$$A\sigma_I + B\sigma_{II} + C\sigma_{III} = 1 \quad (2.44)$$

The ordering of the  $A$ ,  $B$  and  $C$  with the major, intermediate and minor stresses should be

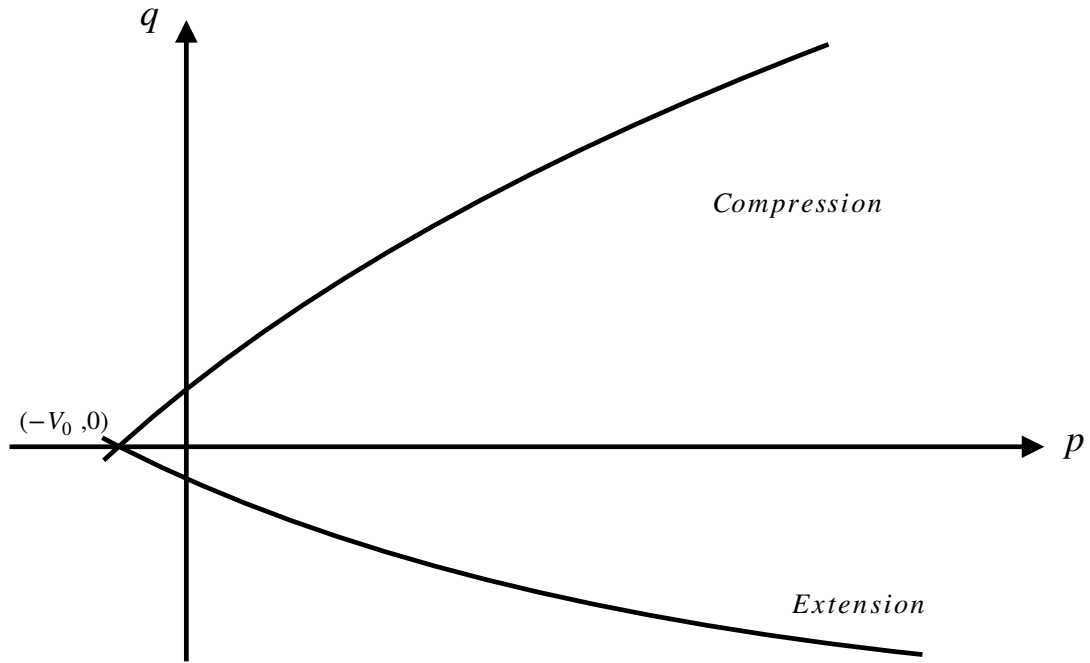


Figure 2.6: Schematic representation of Hoek-Brown criterion failure surface in  $(p - q)$  plane.

kept as defined in Equation 2.44.

Following Meyer and Labuz (2013) [9], the coefficients A, B and C in terms of the rock properties are expressed as:

$$A = \frac{1 - \sin \phi_c}{2V_0 \sin \phi_c} \quad (2.45)$$

$$B = \frac{\sin \phi_c - \sin \phi_e}{2V_0 \sin \phi_e \sin \phi_c} \quad (2.46)$$

$$C = -\frac{1 + \sin \phi_e}{2V_0 \sin \phi_e} \quad (2.47)$$

Equation 2.44 can therefore be written in its complete form as follow:

$$\sigma_I \left[ \frac{1 - \sin \phi_c}{2V_0 \sin \phi_c} \right] + \sigma_{II} \left[ \frac{\sin \phi_c - \sin \phi_e}{2V_0 \sin \phi_e \sin \phi_c} \right] + \sigma_{III} \left[ -\frac{1 + \sin \phi_e}{2V_0 \sin \phi_e} \right] = 1 \quad (2.48)$$

PMC refines failure criterion definition by considering different values of the rock properties. It is shown in Equation 2.48 by the subscripts  $c$  and  $e$ , defining the variables for compression or extension.

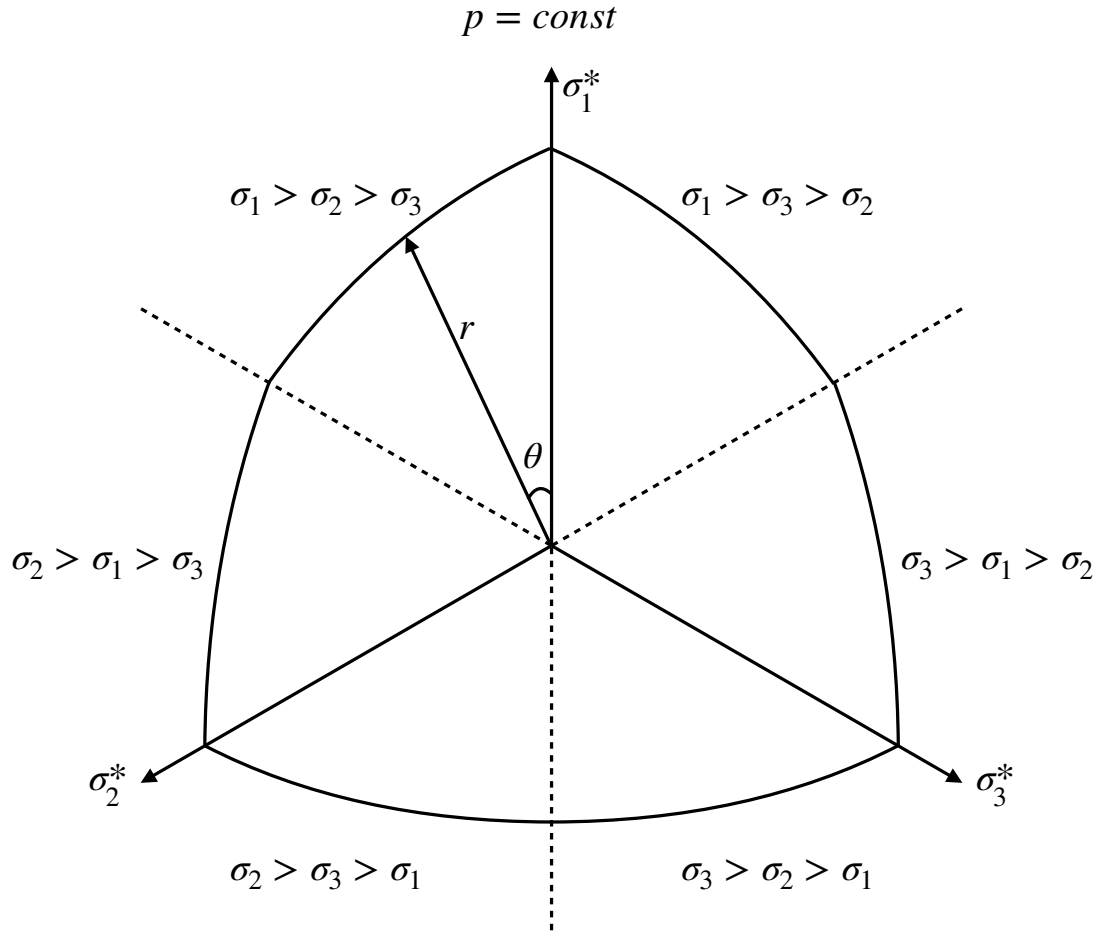


Figure 2.7: Schematic representation of Hoek-Brown criterion failure surface in  $\pi$  plane.

#### Paul-Mohr-Coulomb in the $(\sigma_3 - \sigma_1)$ plane

Paul-Mohr-Coulomb is based on the Mohr-Coulomb criterion, therefore its expression in the  $(\sigma_3 - \sigma_1)$  plane is an adjustment of Equation 2.48 considering different friction angles and cohesion for compression and extension conditions:

$$\sigma_I = M_{c,e} \sigma_{III} + C_{c,e} \quad (2.49)$$

Where:

$$M_{c,e} = \frac{1 + \sin \phi_{c,e}}{1 - \sin \phi_{c,e}} \quad (2.50)$$

$$C_{c,e} = \frac{2c_{c,e} \cos \phi_{c,e}}{1 - \sin \phi_{c,e}} \quad (2.51)$$

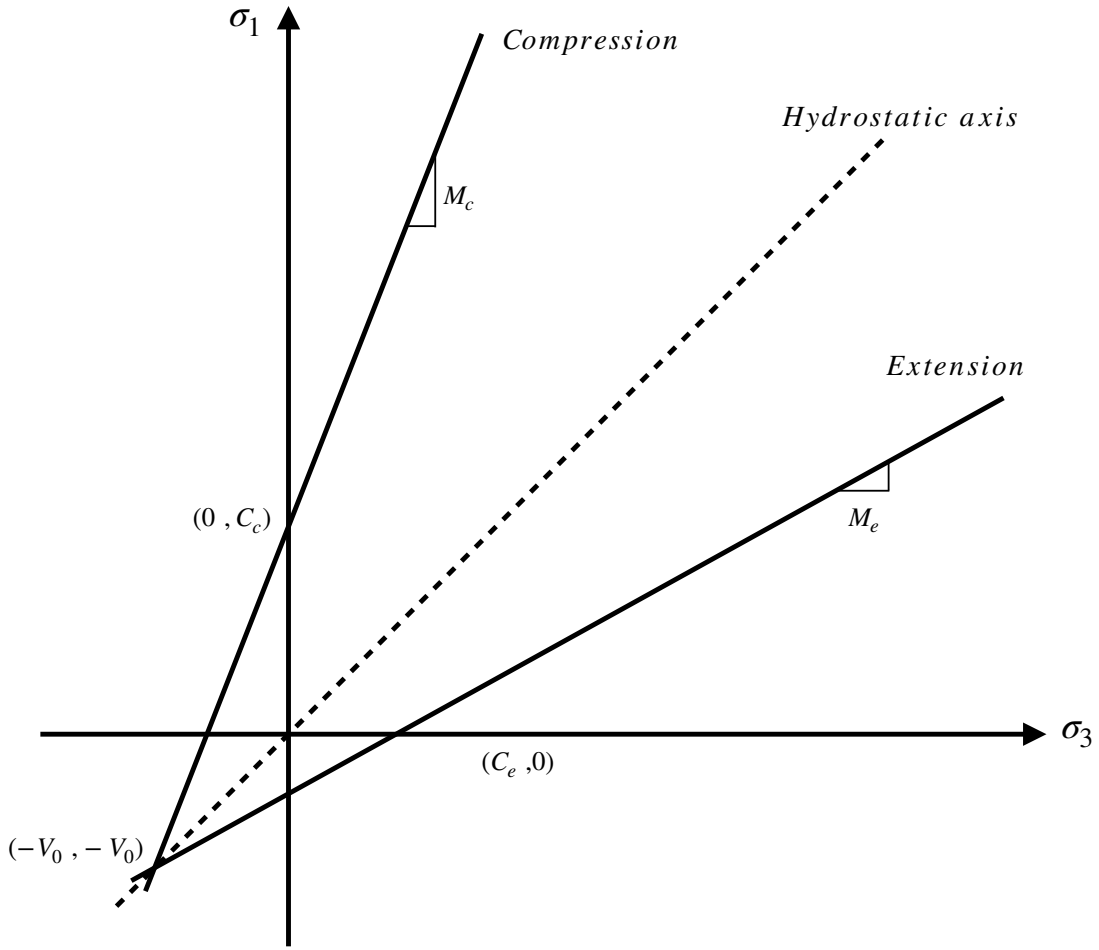


Figure 2.8: Schematic representation of Paul-Mohr-Coulomb criterion failure surface in  $(\sigma_3 - \sigma_1)$  plane.

Paul-Mohr-Coulomb failure surfaces in  $(\sigma_3 - \sigma_1)$  coordinates system are presented in Figure 2.8. As the friction angle and the cohesion for compression and extension are different, Paul-Mohr-Coulomb is not necessarily symmetrical about the hydrostatic axis. The computation of  $V_0$  will be discussed in section 2.3.

#### Paul-Mohr-Coulomb in the $(p - q)$ plane

The PMC in the  $(p - q)$  coordinate system for axisymmetric loading may be defined as:

$$q = \frac{6 \sin \phi_c}{3 - \sin \phi_c} p + \frac{6 c_c \cos \phi_c}{3 - \sin \phi_c} \quad (2.52)$$

$$q = \frac{6 \sin \phi_e}{3 + \sin \phi_e} p + \frac{6 c_e \cos \phi_e}{3 + \sin \phi_e} \quad (2.53)$$

or in the indicial form as:

$$q = m_{c,e} p + b_{c,e} \quad (2.54)$$

where the coefficients  $m_{c,e}$  and  $b_{c,e}$  are defined as follow:

$$m_c = \frac{6 \sin \phi_c}{3 - \sin \phi_c} \quad \text{and} \quad m_e = \frac{6 \sin \phi_e}{3 + \sin \phi_e} \quad (2.55)$$

$$b_c = \frac{6 c_c \cos \phi_c}{3 - \sin \phi_c} \quad \text{and} \quad b_e = \frac{6 c_e \cos \phi_e}{3 + \sin \phi_e} \quad (2.56)$$

Figure 2.3 for Mohr-Coulomb can be used to represent Paul-Mohr-Coulomb criterion after  $m_{c,e}$  and  $b_{c,e}$  recalculated for it.

### **Paul-Mohr-Coulomb in the $\pi$ plane**

The representation of the Paul-Mohr-Coulomb failure criterion in the  $\pi$ -plane is similar to Mohr-Coulomb presented in Figure 2.4. The failure surfaces can be obtained by inserting Equation 2.11 and 2.13 in 2.48. The obtained expressions and their development are presented in Appendix

## **2.3 Paul-Mohr-Coulomb fitting**

Failure criterion are conjectural. They try to provide a mathematical formulation of rock behavior based on experiments. However, the results obtained from them are not direct measurements of the friction angle or cohesion. The data from strength testing give the state of stress at failure. The fitting parameters are computed from these stresses.

The use of the Paul-Mohr-Coulomb requires that the model constants ( $V_0, \phi$ ) be estimated by fitting the Paul-Mohr-Coulomb criterion to the measured data from conventional triaxial compression, conventional triaxial extension, and true triaxial tests. Labuz et al. [1] provide a detailed mathematical derivation of Equations 2.11 to 2.13 that leads to the expression of Paul-Mohr-Coulomb failure criterion in terms of the stress invariants  $p, q$  and  $\theta$ .

Failure criterion fitting consist in the computation of the rock properties ( $V_0, \phi$ ) from a mathematical formulation of the criterion written in terms of the three principal stresses. Labuz (2018) [1] and Folta (2016) [10] provide detailed mathematical derivation of Equations 2.11 - 2.13 that leads to the expression of Paul-Mohr-Coulomb failure criterion in terms of the stress invariants  $p, q$  and  $\theta$ .

### 2.3. Paul-Mohr-Coulomb fitting

---

The final formulation is given by Equation 2.57:

$$q \cos(\theta) = \frac{b_c}{V_0} p + k \sin(\theta) q + b_c \quad (2.57)$$

where:

$$k = \frac{1 - 2\alpha}{\sqrt{3}} \quad (2.58)$$

$$\alpha = \frac{b_c}{b_e} \quad (2.59)$$

Each data point  $i$  from a conventional triaxial or multi-axial experiment is defined by a set of  $(p_i, q_i, \theta_i)$  values. Therefore, for any given data set, Equation 2.57 describes a system of linear equations. This system has  $m$  equations, with  $m$  being the number of experiments performed on the rock. Equation 2.57 can also be written as a matrix equation of the type  $Ax = b$ :

$$\begin{bmatrix} q_1 \cos(\theta_1) \\ \dots \\ q_m \cos(\theta_m) \end{bmatrix} = \begin{bmatrix} p_1 & q_1 \sin(\theta_1) & 1 \\ \dots & \dots & \dots \\ p_m & q_m \sin(\theta_m) & 1 \end{bmatrix} \begin{bmatrix} b_c/V_0 \\ k \\ b_c \end{bmatrix} \quad (2.60)$$

where the matrix  $A$  is  $m$ -by-3, the vector  $b$  has  $m$ -row, and the vector  $x$  has 3-row.

From the system defined in Equation 2.60,  $b_c$ ,  $k$ , and  $V_0$  and can be determined;  $k$  and  $b_c$  are given by the second and third row of parameter vector  $x$ , and  $V_0$  and  $b_e$  are computed as follow:

$$V_0 = \frac{b_c}{x_1} \quad (2.61)$$

$$b_e = \frac{2b_c}{(1 - \sqrt{3}k)} \quad (2.62)$$

The friction angles can be determined by solving Equations for 2.52 and 2.53 for  $q(p = -V_0) = 0$ :

$$\sin \phi_c = \frac{3b_c}{6V_0 + b_c} \quad (2.63)$$

$$\sin \phi_e = \frac{3b_e}{6V_0 - b_e} \quad (2.64)$$

Similarly, the cohesions are obtained for  $q(p = 0) = b_{c,e}$ :

$$c_c = \frac{b_c(3 - \sin\phi_c)}{6\cos\phi_c} \quad (2.65)$$

$$c_e = \frac{b_e(3 + \sin\phi_e)}{6\cos\phi_e} \quad (2.66)$$

# **3 Dunnville sandstone**

This chapter presents a summary of geology, mineralogy and mechanical properties of Dunnville sandstone. The results of simple tests such as uniaxial compression test and conventional triaxial tests on dry specimens are discussed and analyzed.

## **3.1 Geology, mineralogy and properties of the Dunnville sandstone**

In this study, Dunnville sandstone was selected for the laboratory experiments due to its availability, homogeneity and its isotropic behavior (at high mean stress when cracks are closed). Indeed, previous experiments on Dunnville Sandstone showed an isotropic behavior under different conditions of triaxial testing [2]. The following paragraphs provide a short summary of geological and mineralogical properties of Dunnville sandstone.

### **3.1.1 Geological history**

Dunnville sandstone comes from Dunnville, Wisconsin. The quarry is located in a valley at the intersection of the Chippewa river and one of its tributary. Dunnville sandstone constituent materials were deposited during the Cambrian period when Wisconsin was submerged several times by a sea, enabling the deposition of a large amount of sediments. The consolidation and compaction of the deposited materials by glaciers during the Pleistocene Epoch geological time and the subsequent removal of ice due to melting and rise in ambient temperatures led to the development of highly over-consolidated sedimentary rocks in the region (i.e., Dunnville sandstone). Dunnville sandstone is a member of the Elk Mount Formation and particularly the Eau Claire group [11].

### **3.1.2 Mineralogy**

Dunnville Sandstone is composed of 90% of medium-grained quartz and a small amount of cementitious material and may be referred to as a quartz arenite. Other minerals are readily

### Chapter 3. Dunnville sandstone

---



Figure 3.1: Dunnville sandstone mineralogy

noticeable such as orange beds of alkali feldspars and biotite grains (Fig. 3.1). The elongated biotite crystals are disparately distributed in the rock matrix and oriented parallel to the bedding. The mineralogical composition of Dunnville sandstone performed by American Engineering Testing is summarized in Table 3.1 [2]. Dunnville sandstone is a highly porous and permeable rock, with a porosity of 29-30% and permeability of 220 mD [2].

Mineral	Volume [%]
Quartz	90-95
Alkali Feldspar	2-5
Biotite	2-5
Plagioclase	Trace -1
Muscovite	Trace
Clinozoisite	Trace
Zircon	Trace
Hematite	Trace
Iron-oxide	1-2

Table 3.1: Mineralogy of Dunnville Sandstone [2]

The dry density and the P-wave velocity were measured for all specimens tested in this study. The dry density  $\rho$  is  $1910 \pm 30 \text{ kg/m}^3$  and the P-wave velocity  $V_P$  is  $1825 \pm 124 \text{ m/s}$ . The wave travel time for evaluation of the P-wave velocity was measured perpendicular to the bedding planes.

## 3.2 Uniaxial compression test

One uniaxial compression test was performed on Dunnville sandstone to determine Young's modulus  $E_i$  and the uniaxial compressive strength  $C_o$ . These parameters are essential to understand the behavior of the rock and are used for the analysis of behavior in subsequent chapters.

### 3.2.1 Specimen preparation

A cylindrical specimen was ground to ensure the ends were perpendicular to the specimen axis and dried prior to test in accordance with the ISRM suggested methods [12] and ASTM standard [13]. A detailed description of the specimen preparation procedure will be presented in section 3.3.2. The specimen dimensions, with  $h \approx 2d$ , were:  $h = 95.70\text{ mm}$ ,  $d = 50.76\text{ mm}$ . Following Labuz and Bridell (1993) [14], stearic acid was applied to the specimen ends to reduce friction and thereby to minimize the end effects.

### 3.2.2 Procedure

The test was performed using a 1 MN MTS closed loop servo-hydraulic load frame (MTS System Corporation). The uniaxial compression test was stroke controlled to avoid sudden failure of the rock where a displacement rate of  $0.001\text{ mm s}^{-1}$  was used. The displacement of the actuator (stroke) and the force applied to the specimen were recorded during the test.

A small seating load of  $\sim 1 - 2\text{ kN}$  was applied before the test initiated to ensure adequate contact between the loading platens and the specimen. The axial load was then increased until  $\sim 50\%$  of the expected uniaxial compressive strength  $C_0$  of the rock following by unloading to  $\sim 1 - 2\text{ kN}$ . This loading-unloading cycle is used to determine the Young's modulus  $E_i$  of the rock after specimen displacements were corrected for the machine displacement. The axial load was then increased until failure of the rock specimen was achieved. The test was continued until the load decreased to  $\sim 75\%$  of  $C_0$ .

The following stress path describes the uniaxial test:

$$\sigma_1 = \sigma_a \text{ with } \sigma_a > 0 \quad (3.1)$$

$$\sigma_2 = \sigma_3 = \sigma_r \text{ with } \sigma_r = 0 \quad (3.2)$$

### 3.2.3 Results

From the recorded axial displacement and force, the axial stress and the axial strain can be computed:

$$\sigma_a = \frac{F_a}{A} \quad (3.3)$$

$$\epsilon_a = \frac{u}{h} \quad (3.4)$$

Where:

$\sigma_a$  : axial stress [MPa]

$\epsilon_a$  : axial strain [-]

$A = \frac{d\pi^2}{4}$  : cross section area of the cylindrical specimen [mm<sup>2</sup>]

$F_a$  : axial load applied through the load frame [N]

$u$  : axial displacement corrected for machine displacement [mm]

$h$  length of the specimen [mm]

Fig 3.2 present the stress-strain plot obtained from the uniaxial compression test. The uniaxial compressive strength of the rock specimen is calculated as:

$$C_o = \frac{F_{\text{peak}}}{A} = \sigma_{a,\text{peak}} = 29.83 \text{ MPa} \quad (3.5)$$

Young's modulus of the rock is computed using the loading-unloading cycle:

$$E = \frac{\Delta\sigma}{\Delta\epsilon} = 5860 \text{ MPa} \quad (3.6)$$

Fig 3.3 presents the specimen after the test. The failed specimen showed axial splitting and a failure surface with a conical shape.

### 3.3 Conventional triaxial tests

Shear strength of Dunnville sandstone was determined using conventional (axisymmetric) triaxial tests (CT). Two types of CT tests were performed, namely, the conventional triaxial compression (CTC) and the conventional triaxial extension (CTE). For these tests, two of the principal stresses are equal. The state of stress of the rock specimen is then simplified to the axial stress  $\sigma_a$  and the radial stress  $\sigma_r$ .



Figure 3.2: Stress and Strain relationship for the uniaxial compression test

### 3.3.1 Hoek-Franklin cell

A Hoek -Franklin pressure cell was used to perform the conventional triaxial tests [15]. The maximum capacity of the cell is 69 MPa and allows the independent application of axial and radial stresses. The device is composed of a pressure vessel, a synthetic rubber membrane and two loading platens (Fig 3.4).

The radial stress was applied using a fluid pressure system where confinement is provided using hydraulic oil. The fluid pressure system is composed of a microcontroller and a screw-type hydraulic intensifier that allows for confining pressure to be held constant throughout the test. The axial load is applied through steel platens with a 1 MN MTS servo-hydraulic load frame (MTS System Corporation). The monitoring of the axial displacement and axial force are done using a data acquisition system (Fig 3.5).

A rubber membrane was used to isolate the specimen and the loading platens from the confining fluid, and to allow for radial and axial stresses to be applied independently. The membranes used herein have an inner diameter of 32.0 mm and are 85.0 mm in height (Fig 3.6).



Figure 3.3: Stress and Strain relationship for the uniaxial compression test

### 3.3.2 Specimen preparation

Rock cores were obtained from a block of Dunnville sandstone. The specimens were prepared following ASTM Standard Practice D4543-19 [13]. In preparation of the test specimens, particular attention was given to (i) the straightness of the elements on the cylindrical surface, (ii) flatness of the end bearing surfaces and (iii) perpendicularity of the end surfaces with the respect to axis of the core. The following describes the procedure used in preparation of the specimens:

1. *Cutting and grinding of the end surfaces:* for the purpose of sealing, the specimen dimensions should match that of the cell membrane. The core diameters ranged from 30.2 mm to 30.6 mm. The specimens were cut using a diamond saw and ground using a carborundum grinding wheel. A precision table was used to ensure that specimen ends were perpendicular to the specimen axis. The final height  $h$  of the specimens ranged from 75.7 mm to 81.8 mm
2. *Drying:* all the specimens were oven dried at 150 °C for at least 24 hours before the tests to ensure dry conditions existed during the triaxial tests
3. *Minimizing end friction:* the ends and cylindrical surface of the specimens were coated with stearic acid [13]. This lubricant was used to reduce frictional effects between the membrane and the specimen.

In addition to standard preparation, one specimen (TC 9 at  $\sigma_r = 5.0 \text{ MPa}$ ) was equipped with a strain gages rosette where axial and transverse strains were measured (Fig 3.7). The procedure for gluing the strain gage set was executed with much care to avoid damaging the gages. All the tools used in the process were cleaned with acid and neutralizer before touching the strain gage. Due to the high porosity of the Dunnville sandstone, the surface of the rock was coated



Figure 3.4: Hoek-Franklin cell

with the same epoxy that was used to attach the gage. The surface of the specimen was then cleaned using xylene and the strain gage was attached using M-Bond 200 epoxy adhesive.

### 3.3.3 Conventional triaxial compression test

The following procedure was followed to setup and conduct the conventional triaxial compression tests:

1. The specimen was inserted in the Hoek-Franklin cell. The cell was held in a horizontal position and hydraulic oil was inserted to ensure no entrapped air existed in the annulus between the cell walls and the membrane.
2. The pressure cell-specimen-loading platen assembly was then placed inside the load frame and seating stress of  $\sigma_a \approx 1 \text{ MPa}$  was applied to the specimen to ensure adequate contact between the specimen and the platens. To ensure small deviatoric stresses,  $\sigma_r \approx 1 \text{ MPa}$  was applied. It is noted that this condition corresponds to a hydrostatic stress state ( $\sigma_a = \sigma_r = 1 \text{ MPa}$ ).
3. The axial ( $\sigma_a$ ) and radial ( $\sigma_r$ ) stresses were then increased hydrostatically until the desired confining pressure ( $\sigma_r$ ) was achieved. In so doing, a stress increment of  $\sim 5.0 \text{ MPa}$  was consistently used.
4. Once the desired radial pressure  $\sigma_r$  was reached, the deviatoric loading was initiated by



Figure 3.5: Conventional triaxial test set up

maintaining the radial stress ( $\sigma_r$ ) constant while axial stress ( $\sigma_a$ ) were increased until failure was achieved. It is noted that all tests were stroke controlled with a displacement rate of  $0.001 \text{ ms}^{-1}$ . The stress path applied during the test can be summarized as follow:

$$\sigma_1 = \sigma_a \text{ with } \sigma_a > 0 \quad (3.7)$$

$$\sigma_2 = \sigma_3 = \sigma_r \text{ with } \sigma_r = 0 \quad (3.8)$$

$$\sigma_a > \sigma_r \quad (3.9)$$

### 3.3.4 Conventional triaxial compression test

The following procedure was followed to setup and run the conventional triaxial extension tests:

1. The same device and tests preparation, as those previously explained for the conventional triaxial compression tests, were used for the conventional triaxial extension tests (see steps 1-3 in Section 3.3.3).



Figure 3.6: Membrane hosting the rock specimen in the Hoek-Franklin cell

2. In a conventional triaxial extension test, however, the axial stress is decreased as opposed to increasing the axial stress in triaxial compression tests.
3. This test was stroke controlled with displacement rate of  $0.001 \text{ m s}^{-1}$ . The radial stress was kept constant at the desired confining pressure using the hydraulic intensifier, while the axial stresses decreased through the displacement of the load frame. The stress path applied during the test can be summarized as follow:

$$\sigma_1 = \sigma_2 = \sigma_r \text{ with } \sigma_r = 0 \quad (3.10)$$

$$\sigma_3 = \sigma_a \text{ with } \sigma_a < 0 \quad (3.11)$$

$$\sigma_a < \sigma_r \quad (3.12)$$

#### 3.3.5 Results

Five conventional triaxial compression tests ( $\sigma_r = 5, 10, 20, 40$  and  $60 \text{ MPa}$ ) and three conventional triaxial extension tests ( $\sigma_r = 35, 40$  and  $60 \text{ MPa}$ ) were performed. The test results are summarized in Table 3.2 and the stress-strain relationships for all tests are shown in Fig 3.8

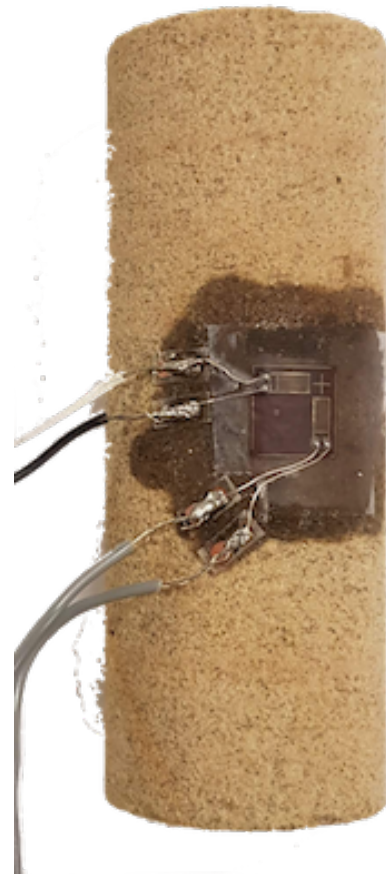


Figure 3.7: Strain Gage set up on a CTC specimen

### Conventional triaxial compression tests

**Stress vs. strain plot** From 0 MPa to 20 MPa of confining stress, the rock is in the brittle domain as the axial stress is dropping after reaching maximal axial stress. At higher confining pressures ( $\sigma_r > 40$  MPa and  $\sigma_r < 60$  MPa), however, rock is transitioning from a brittle to ductile response as represented by the post-peak drop in stresses as seen in Fig. 3.8. Finally, the rock shows a ductile behavior under a confining stress of 60 MPa, where the axial stress does not reach a peak value.

**Mohr circles plot** The conventional triaxial compression results can also be presented on a Mohr plane, where the Mohr circles and the non-linear failure envelope are shown (Figure 3.9). This plot indicates that the friction angle for Dunnville sandstone is stress dependent and cannot be represented using the Mohr-Coulomb linear failure envelope for the entire range of possible stress states. The nonlinear failure envelope, however, may be linearized over small stress intervals as shown in Fig 3.9. The corresponding Mohr-Coulomb strength parameters (friction angle  $\phi$  and cohesion intercept  $c$ ) are summarized in Table 3.3.

### 3.3. Conventional triaxial tests

Test	$\sigma_1$ [MPa]	$\sigma_2$ [MPa]	$\sigma_3$ [MPa]	$p$ [MPa]	$q$ [MPa]	$\theta$ [°]	$E_i$ [MPa]
TC 9	49.43	5	5	19.81	44.43	0	5861
TC 0	61.43	10	10	27.95	51.43	0	6407
TC 5	91.08	20	20	44.72	71.08	0	7014
TC 8	127.3	40	40	65.73	87.30	0	6687
TC 10	151.1	60	60	88.12	91.10	0	6842
TE 3	35	35	3.96	24.64	31.08	60	7922
TE 1	40	40	4.50	27.89	36.34	60	8390
TE 2	60	60	9.68	43.01	50.98	60	8695

Table 3.2: Summary of CTC and CTE tests results

Segment	[ $\phi$ °]	$c$ [MPa]
5 – 10 MPa	30.73	9.67
10 – 20 MPa	29.37	10.42
20 – 40 MPa	14.41	23.6
40 – 60 MPa	4.72	36.94

Table 3.3: Mohr-Coulomb strength parameters for various stress regimes for Dunnville sandstone

**Poisson's ratio** Poisson's ratio of Dunnville sandstone was computed using the results of the axial and radial strains for specimen TC 9:

$$\nu = \frac{-\epsilon_{\text{radial}}}{\epsilon_{\text{axial}}} = 0.26 \quad (3.13)$$

Fig 3.10 shows a plot of the radial strain vs. the axial strain measured during the test.

**Failure surfaces** Table 3.4 presents pictures of the CTC tests specimens after failure, where failure surfaces are observable. In ideal conditions with no friction at the interface with the applied stress, the specimen should show splitting in the direction of the major stress (Figure 3.11). Although the interface between the specimens and the platens was lubricated using stearic acid, some friction remained, and a majority of the tested specimens shows failure angles of  $\sim 60^\circ$ . The specimen tested at a confining pressure of 60 MPa shows multiple fractures at the top and bottom, as well as horizontal splitting. At this value of confining stress, the rock behavior becomes ductile and begins to yield, leading to compaction of the solids constituting it.

#### Conventional triaxial extension tests

**Stress vs. strain plot** Fig 3.8 presents the axial stress vs. axial strain curves for the extension tests. The axial stress in the figure represent the amount of axial stress that is removed from

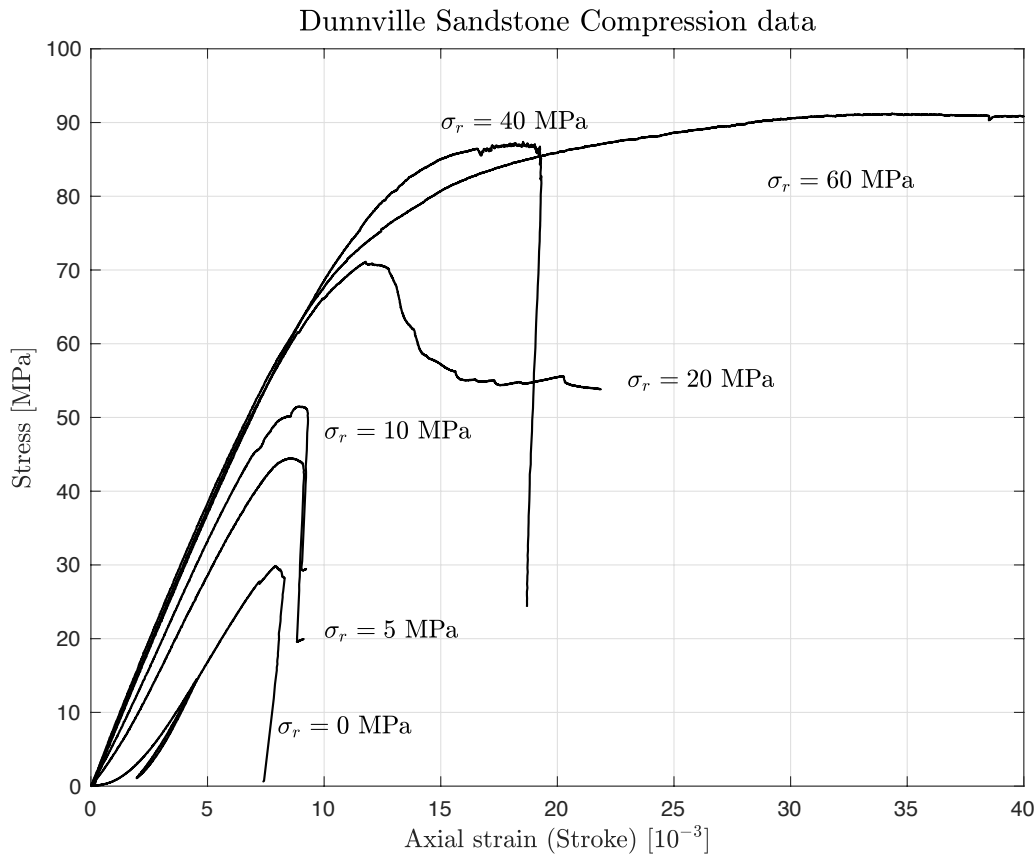


Figure 3.8: Summary of the stress-strain relationships for the triaxial compression and extension tests

the original hydrostatics state of stress. In order to find the axial stress at failure, the following formula is used:

$$\sigma_{\text{failure}} = \sigma_{a,\text{removed}} - \sigma_r \quad (3.14)$$

**Failure surfaces** Table 3.5 presents pictures of the CTE tests specimens after failure. In ideal conditions with no friction at the interface with the applied stress, the specimen should show splitting in the direction of the major stress (Figure 3.11). The tested specimens show failure angles close to horizontal splitting. The small deviation from this ideal condition can be explained by a remaining friction between the membrane and the specimen, and the localized anisotropy, as failure seems to follow the bedding planes orientation.

### 3.3. Conventional triaxial tests

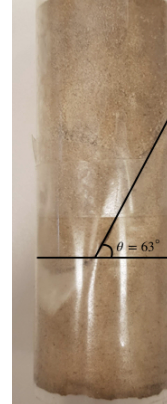
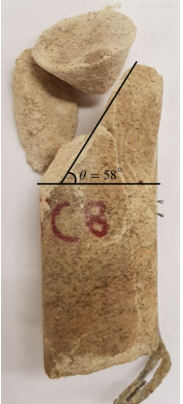
$\sigma_r = 5 \text{ MPa}$	$\sigma_r = 10 \text{ MPa}$	$\sigma_r = 20 \text{ MPa}$	$\sigma_r = 40 \text{ MPa}$	$\sigma_r = 60 \text{ MPa}$
				
$\theta = 66^\circ$	$\theta = 63^\circ$	$\theta = 57^\circ$	$\theta = 58^\circ$	$\theta \approx 0^\circ$

Table 3.4: Failure surfaces for conventional triaxial compression tests

$\sigma_r = 35 \text{ MPa}$	$\sigma_r = 40 \text{ MPa}$	$\sigma_r = 60 \text{ MPa}$
		
$\theta = 10^\circ$	$\theta = 0^\circ$	$\theta = 27^\circ$

Table 3.5: Failure surfaces for conventional triaxial extension tests

### Chapter 3. Dunnville sandstone

---

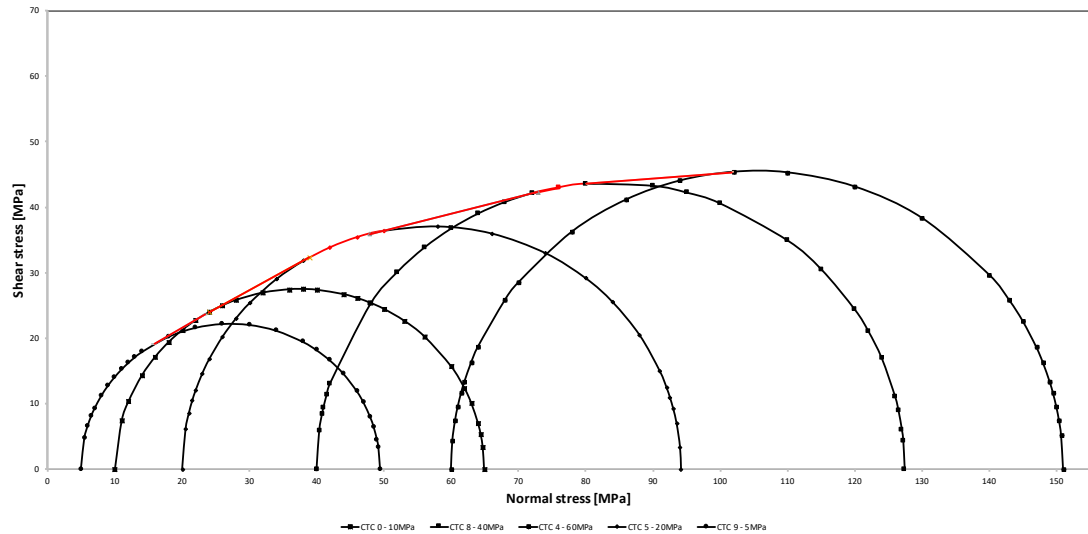


Figure 3.9: Mohr-Coulomb circles for the conventional triaxial compression tests.

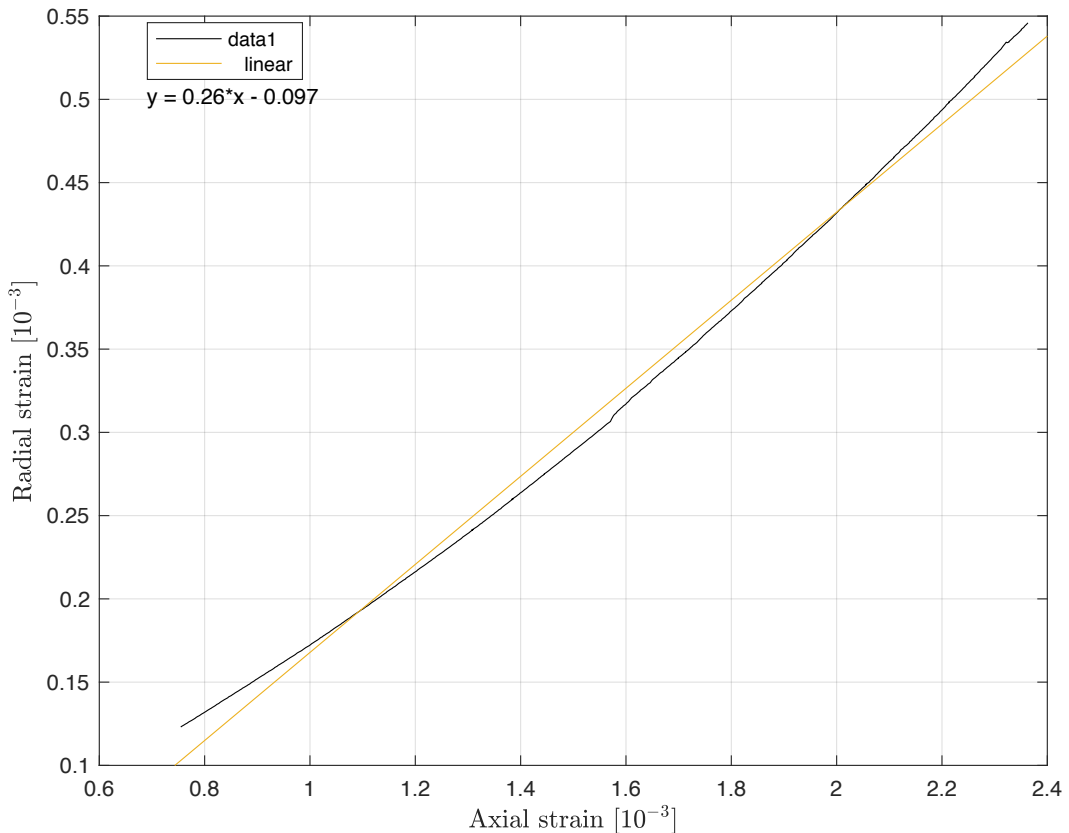


Figure 3.10: Poisson's ratio of Dunnville sandstone

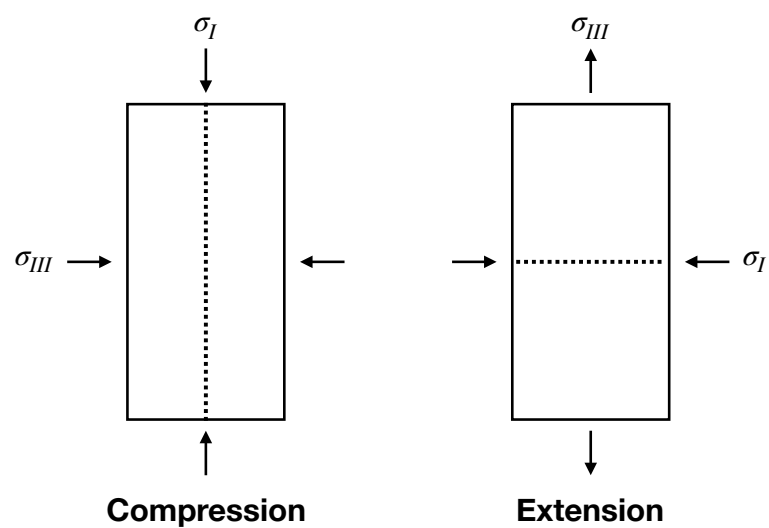


Figure 3.11: Theoretical specimen failure



# 4 Multi-axial experiments

The development of a successful failure criterion requires experiments and particularly multi-axial testing [1] to be performed. These tests are needed to provide material performance at various stress states, e.g. to assess the intermediate principal stress effect and to enrich the database used to calibrate failure criteria. This chapter presents the multi axial experiments performed for this study.

## 4.1 Introduction

The development of failure criteria requires a diversity of experiments to be the representative of the rock behavior. Axisymmetric or conventional triaxial experiments, presented in Chapter 3, are typical laboratory techniques performed as a first approach to determine strength parameters. Although they are convenient to perform, the principal stresses cannot be varied independently; two principal stresses are always equal. To address this issue, true triaxial testing was developed to represent the in-situ stress state underground, by creating “true triaxial” testing conditions that simulate three-dimensional states of stress [1].

In addition to the three-dimensional state of stress, many geo-engineering problems approximate a plane state of strain. It is particularly the case for tunnels and other long structures with a constant cross-section and loaded in the plane of the cross-section [4]. Although plane strain is a reasonable model of reality, the condition is challenging to reproduce in experiments. Indeed, on top of independent application of the three principal stresses, the plane-strain condition requires a precise control of the strain in the intermediate stress direction, as it should be equal to zero for the duration of the test.

In this study, the Plane-Strain Apparatus developed by Labuz et al. (1996) [6] was selected to perform experiments on Dunnville Sandstone, as it enables experiments to be performed under a three-dimensional stress state, with the option of restricting strain in one direction.

## **4.2 Multi-axial apparatus**

The University of Minnesota Plane-Strain Apparatus enables independent application of the principal stresses, using a stiff biaxial frame to induce the intermediate stress through passive restraint [6]. Recent modifications of the device enable control and monitoring of the three stresses [3].

### **4.2.1 Development of the apparatus**

The Plane-Strain Apparatus (US Patent number 5 063 785), was first designed based on a passive, stiff frame concept. The device enabled testing of rock specimen under plane strain conditions with active application of the major and minor stresses, and passive restraint for the intermediate stress through the biaxial frame [6].

The apparatus was recently improved with the addition of two hydraulic pistons acting in the intermediate principal stress direction which enable the active application and control of major, intermediate and minor stresses [3]. This device allows failure surfaces to develop and propagate in an unrestricted manner, unlike conventional triaxial compression where the specimen is constrained by the loading platens. In short, the Plane-Strain Apparatus gives the possibility to simulate in-situ conditions of rock underground.

### **4.2.2 Description of the apparatus**

The apparatus can be defined as a pressure cell made of four components, each one related to a particular feature of the testing conditions [6, 3].

**Base unit** The base unit is equipped with high-pressure pass throughs designed to receive in-vessel instrumentation such as LVDTs (Linear Variable Differential Transformer), strain gages, and an internal load cell, above which specimen is placed. Figure 4.1 shows the base unit and denotes its components.

**Biaxial frame** The biaxial frame was designed to bring maximum possible stiffness to the apparatus when it was used as passive restraint to restrict deformation of the specimen. It is now hosting the hydraulic pistons, with a maximum capacity of 69 MPa, that directly induce the intermediate stress. The frame is placed so that the pistons are aligned with the lateral platens fixed to the specimen. Two holes were machined in the frame to allow placement of the lateral LVDTs. Figure 4.2 shows the biaxial frame and denotes its components.

**Loading piston assembly** The loading piston assembly combines two features of the apparatus. It is used to apply the axial load to the specimen and enables the failure surface to

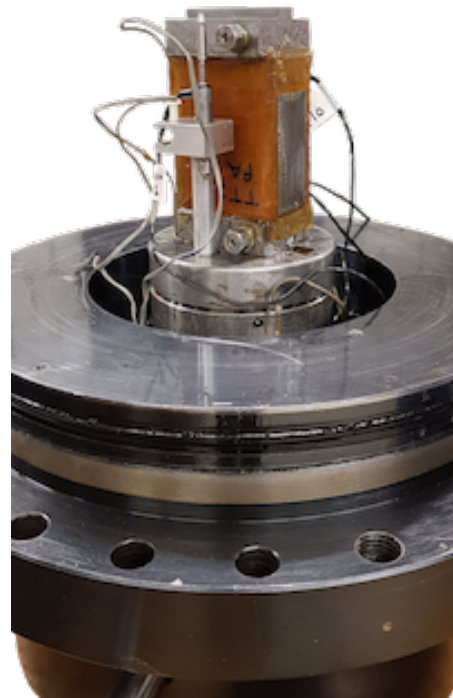


Figure 4.1: Base unit of the Plane-Strain Apparatus

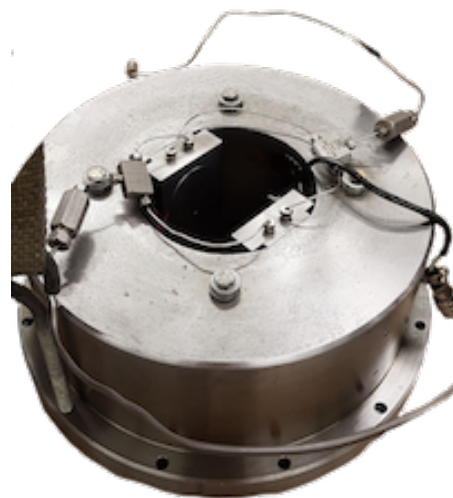


Figure 4.2: Biaxial Frame of the Plane-Strain Apparatus

develop and propagate freely in the minor stress direction. It is composed of a linear bearing, bolted to the bottom of the loading piston, which can slide over a trackway when a mechanism forms. The loading piston maximum capacity is 500 MPa. Figure 4.3 shows the loading piston assembly and denotes its components.

**Pressure vessel** The four elements presented are placed in a pressure vessel designed to hold the pressurized fluid used to apply the minor stress. The top cap and base pot are bolted to the pressure vessel surrounding the apparatus. The maximum capacity is 24 MPa. Figure 4.4 shows the pressure vessel and denotes its components.

### 4.3 Specimen preparation

The concept of multi axial testing involves the use of a prismatic specimen. Indeed, in order to respect their independence, each of the three principal stresses have to be applied perpendicular to the specimen surface. The specimen preparation included geometric adjustments, instrumentation with strain gages, and jacketing.

#### 4.3.1 Dimensions

The theoretical dimensions of the specimen used for true-triaxial testing in the Plane-Strain Apparatus are presented in the Figure 4.5.

Four prismatic specimens were obtained from a block of Dunnville sandstone to minimize variation in properties. In preparation of the test specimens, particular attention was given to (i) the straightness of the elements on the cylindrical surface, (ii) flatness of the end bearing surfaces and (iii) perpendicularity of the end surfaces with the respect to axis of the core. In order to adjust the dimensions and to ensure (i), (ii) and (iii), the specimens were ground according to the ISRM suggested methods [12] and the ASTM standard [13]. A detailed description of the specimen preparation procedure is presented in section 3.3. The final dimensions for the four specimens tested were:  $h = (69 \pm 1)$  mm,  $L = (60 \pm 1)$  mm,  $b = (30.0 \pm 0.5)$  mm.

The true-triaxial experiments, in the Plane Strain Apparatus, are performed on dry specimens (drained conditions). After the geometry adjustment, the specimens were oven dried for 24 hours at 100 °C.

#### 4.3.2 Specimen instrumentation

Strain measurements in the three principal directions are needed to analyze the volume change behavior of the rock specimen during the experiment. These measurements were made using strain gages as part of the instrumentation setup for multi axial tests.

One face of the specimens was equipped with a pair of strain gages made of one for axial strain

#### **4.3. Specimen preparation**

---



Figure 4.3: Loading piston of the Plane-Strain Apparatus



Figure 4.4: Pressure cell of the Plane-Strain Apparatus

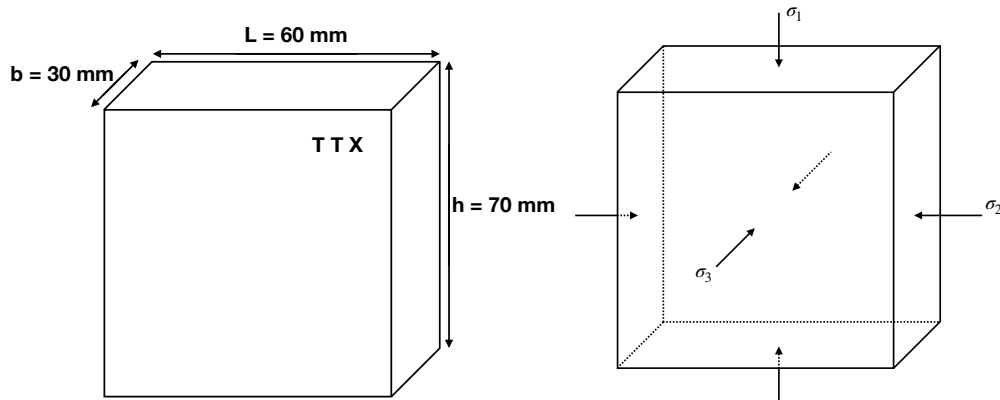


Figure 4.5: a. Specimen dimensions and b. loading directions



Figure 4.6: Specimen instrumented with axial and transversal strain gages

and the other for transversal strain measurements. The set-up procedure is the same as the one described in section 3.3. Once the strain gages were fixed (24 hours of drying), the lead wires were soldered. Figure 4.6 shows the instrumentation of specimen "TT2".

#### 4.3.3 Jacketing

During an experiment in the Plane-Strain Apparatus, the specimen and the instrumentation are immersed in oil used to apply one of the lateral stresses. As the true-triaxial experiments were performed under drained conditions, the specimen needed to be dry (drained) for the duration of the test.

The specimen is protected from the oil by a polyurethane membrane that include the top, bottom and lateral platens in contact with the specimen (Figure 4.7a). It is done to prevent any leakage of oil inside the sample that could lead to a loss of strength for the specimen,

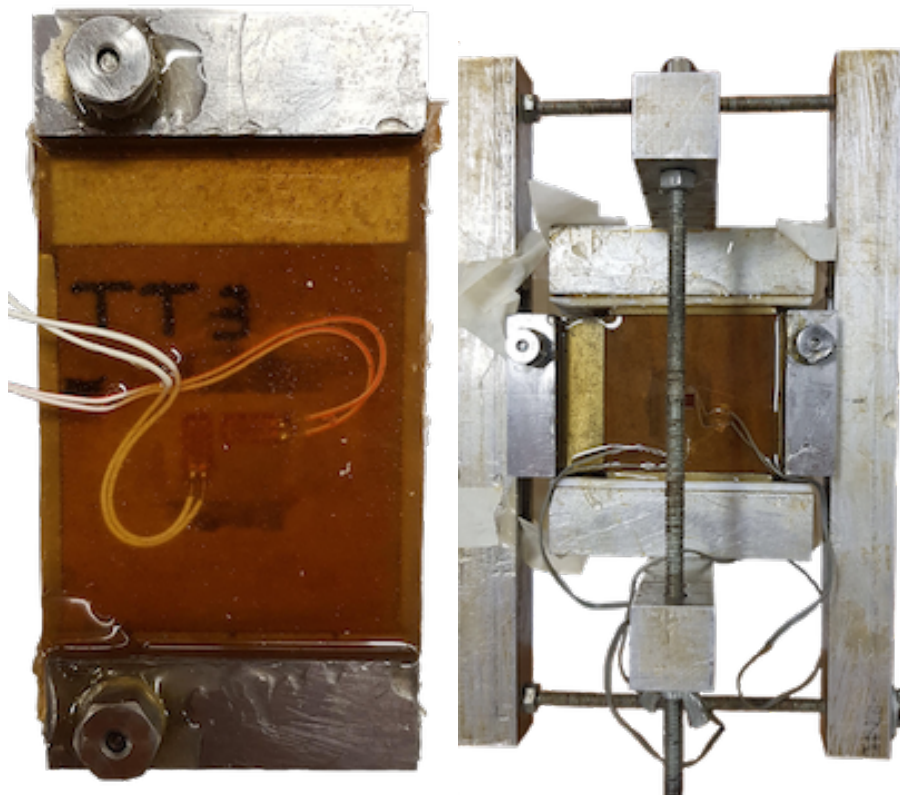


Figure 4.7: a) Jacketed specimen and b) coating set-up

which makes it an important but also challenging step of the experiment setup. The following coating procedure was applied:

1. The upper, lower, and lateral platens were put in contact with the instrumented specimen and held together using clamps (Figure 4.7b)
2. Each face of the specimen was covered with two layers of polyurethane; each dried for 24 hours at room temperature

## **4.4 Experiments**

Although the apparatus was designed about 30 years ago, the loading pistons were recently added to the biaxial frame. This new feature gave the possibility to explore new experiments conditions offered by the Plane-Strain Apparatus. Four tests were performed under different testing conditions and configuration of the equipment.

### 4.4.1 True-triaxial testing

Since the Plane-Strain Apparatus was improved with hydraulic pistons, several true triaxial experiments, particularly under constant mean stress conditions were performed. However, none were done under plane strain conditions. One of this study objectives was to perform the first true triaxial experiment under plane strain condition in the Plane-Strain Apparatus.

#### Apparatus set-up

1. The specimen, coated with polyurethane, was placed on the internal load cell and the position of the axial LVDTs was adjusted. The three LVDTs and the strain gages were connected to high-pressure pass throughs located on the base unit.
2. The biaxial frame was then placed on the base unit, around the specimen, and the loading piston assembly put on top of the specimen and adjusted so that it was centered with the base unit. A LVDT was then attached to the linear bearing (Figure 4.8).
3. The pressure vessel was placed around the assembly, bolted with the base unit and filled with oil.
4. Finally, the top cap was connected to the pistons' hydraulic circuit and bolted to the pressure vessel.

#### Plane strain condition

The plane strain testing condition involves control of the strain in the intermediate stress direction. As the axial (i.e. major) stress increases until failure, the intermediate stress should constantly be adjusted during the test to keep the strain constant and equal to zero in its direction.

The following procedure was applied to perform the true-triaxial experiment under the plane strain condition:

1. The Plane-Strain Apparatus was assembled, placed inside the MTS load frame the instrumentation was connected to the data acquisition system.
2. The hydraulic intensifiers were connected to the pressure cell and the pistons. Each one was bled to ensure no entrapped air existed in the hydraulic circuit.
3. Seating stresses of  $\sigma_1 = \sigma_2 \approx 1 \text{ MPa}$  were applied to the specimen to ensure adequate contact between the specimen and the platens. A  $\sigma_3 \approx 1 \text{ MPa}$  was also applied. It is noted that this condition corresponds to a hydrostatic stress state ( $\sigma_1 = \sigma_2 = \sigma_3 = 1 \text{ MPa}$ ).



Figure 4.8: Apparatus set-up for the true-triaxial experiments

4. The three principal stresses were then increased hydrostatically until the desired confining pressure ( $\sigma_3$ ) was achieved. In so doing, a stress increment of  $\sim 2$  MPa was consistently used. A small deviatoric stress of about 1 MPa was kept during the hydrostatic loading to ensure good contact between the platens and the specimen.
5. Once the desired confining pressure (i.e. minor stress  $\sigma_3$ ) was reached, the deviatoric loading was initiated by maintaining the minor stresses ( $\sigma_3$ ) constant while the major stress ( $\sigma_1$ ) was increased until failure was achieved. The intermediate stress was manually applied and controlled so that the strain in the intermediate stress direction ( $\epsilon_2$ ) was kept constant and equal to zero during the test. The stress path applied during the test can be summarized as follow:

$$\sigma_1 > 0, \quad \Delta\sigma_3 = 0 \quad \text{and} \quad \epsilon_2 = 0 \quad (4.1)$$

## **Chapter 4. Multi-axial experiments**

---

The minor stress was applied using a fluid pressure system where confinement is provided using hydraulic oil. The fluid pressure system is composed of a microcontroller and a screw-type hydraulic intensifier that allows for confining pressure to be held constant throughout the test. A second hydraulic intensifier was used to apply the intermediate stress through the hydraulic pistons. The major stress was applied through the loading piston with a 1 MN load frame.

During the test, the following measurements were recorded:

- Internal load applied to the specimen
- Axial displacement of the specimen
- Axial and transversal strain of the specimen
- Fluid pressure applied to the specimen ( $\sigma_3$ )
- Fluid pressure applied to the pistons ( $\sigma_2$ )
- Displacement of the linear bearing

It is noted that the test was axial displacement controlled using a displacement rate of  $0.0005 \text{ ms}^{-1}$  which was monitored from the average of the two axial LVDTs.

### **Constant mean stress condition**

In order to compare the results given by the plane strain test, a true-triaxial experiment under constant mean stress condition was performed at the mean stress achieved at failure under plane strain condition.

The following procedure was applied:

1. The Plane-Strain Apparatus was assembled, placed inside the MTS load frame the instrumentation was connected to the testing system.
2. The hydraulic intensifiers were connected to the pressure cell and the pistons. Each one was bled to ensure no entrapped air existed in the hydraulic circuit.
3. Seating stresses of  $\sigma_1 = \sigma_2 \approx 1 \text{ MPa}$  were applied to the specimen to ensure adequate contact between the specimen and the platens. A  $\sigma_3 \approx 1 \text{ MPa}$  was also applied. It is noted that this condition corresponds to a hydrostatic stress state ( $\sigma_1 = \sigma_2 = \sigma_3 \approx 1 \text{ MPa}$ ).
4. *Hydrostatic loading phase:* The three principal stresses were then increased hydrostatically until the desired confining pressure ( $\sigma_3$ ) was achieved. In so doing, a stress increment of  $\sim 2 \text{ MPa}$  was used.

5. “*Deviatoric*” loading phase 1: Once the desired confining pressure (i.e. minor stress  $\sigma_3$ ) was reached, the deviatoric loading was initiated by maintaining the minor stresses ( $\sigma_3$ ) constant while the major ( $\sigma_1$ ) and intermediate ( $\sigma_2$ ) stresses were increased to the same value corresponding to the desired mean stress. The stress path applied during the phase can be summarized as follow:

$$\sigma_1 = \sigma_2 = \sigma_{1,2} \text{ with } \sigma_{1,2} = 0 \quad (4.2)$$

$$\Delta\sigma_3 = 0 \quad (4.3)$$

6. “*Deviatoric*” loading phase 2: Once the desired mean stress was reach, it was kept constant during the rest of the test. To do so, the minor stress was kept constant and the major and intermediate stresses followed  $\Delta\sigma_1 = -\Delta\sigma_2$  until failure was achieved.

The lateral stresses were applied using two hydraulic intensifiers connected to the pressure vessel and the pistons. The major stress was applied through the loading piston with a 1 MN load frame.

During the test, the following measurements were recorded:

- Internal load applied to the specimen
- Axial displacement of the specimen
- Axial and transversal strain of the specimen
- Fluid pressure applied to the specimen
- Fluid pressure applied to the pistons
- Displacement of the linear bearing

It is noted that the test was axial displacement controlled using a displacement rate of  $0.0005 \text{ m s}^{-1}$ , which was monitored from the average of the two axial LVDTs.

### 4.4.2 Axisymmetric triaxial compression experiment on a prismatic specimen

One of the specimens prepared for an experiment under constant mean stress condition was too large to fit the biaxial frame. As the specimen preparation is time consuming, it was decided to modify the Plane-Strain Apparatus, by removing the biaxial frame, and to perform an axisymmetric triaxial compression test on a prismatic specimen.

In this configuration, the apparatus preserved the base unit, the loading piston and the pressure cell. The axial (major) stress was still applied by the loading piston and the intermediate



Figure 4.9: Apparatus set-up for the axisymmetric triaxial experiment on a prismatic specimen

stress was induced through fluid pressure, equal to the minor stress. The stress state that undergoes the specimen during this experiment was similar to the one applied in conventional triaxial compression.

#### **Apparatus set-up**

For this experiment, the Plane-Strain Apparatus configuration was modified by removing the biaxial frame. In addition to the usual elements of the device, three steel cylinders equipped with threaded rod were placed between the base unit and the loading piston assembly (Figure 3.9).

In the standard configuration of the device, the biaxial frame acts as an emergency stop that protects the instrumentation below the loading piston, in case of a sudden drop of the assembly due to brittle failure of the specimen. However, in this axisymmetric triaxial testing set-up, nothing stands between the base unit and the loading piston. The three cylinders were then added to the apparatus to replace the biaxial frame and avoid damaging

the instrumentation around the specimen. The height was adjusted in order to have a less than 5 mm spacing with the loading piston, which correspond to the displacement range of the LVDTs placed next to the specimen.

As more space was available around the specimen, lateral LVDTs were also added to measure displacement and strain in the minor stress direction.

#### **Procedure**

The procedure defined for conventional triaxial compression in Chapter 3 was followed for this experiment:

1. The Plane-Strain Apparatus was assembled and placed inside the MTS load frame.
2. A seating stress of  $\sigma_a \approx 1 \text{ MPa}$  was applied to the specimen to ensure adequate contact between the specimen and the platens. It is noted that this condition corresponds to a hydrostatic stress state ( $\sigma_r = \sigma_a \approx 1 \text{ MPa}$ ).
3. The axial ( $\sigma_a$ ) and radial ( $\sigma_r$ ) stresses were then increased hydrostatically until the desired confining pressure ( $\sigma_r$ ) was achieved. In so doing, a stress increment of  $\sim 2 \text{ MPa}$  was consistently used.
4. Once the desired confining pressure (radial stress  $\sigma_r$ ) was reached, the deviatoric loading was initiated by maintaining the radial stresses ( $\sigma_r$ ) constant while the axial stress ( $\sigma_a$ ) was increased until failure was achieved. The stress path applied during the test can be summarized as follow:

$$\sigma_1 = \sigma_a \text{ with } \sigma_a > 0 \quad (4.4)$$

$$\sigma_2 = \sigma_3 = \sigma_r \text{ with } \sigma_r = 0 \quad (4.5)$$

$$\sigma_a > \sigma_r \quad (4.6)$$

$\sigma_1$ ,  $\sigma_2$  and  $\sigma_3$  are the principal stresses of the stress state; respectively major, intermediate and minor stress.

The radial stress was applied using a fluid pressure system where confinement is provided using hydraulic oil. The axial load was applied through the loading piston with a 1 MN MTS load frame.

During the test, the following measurements were recorded:

- Internal load applied to the specimen

## Chapter 4. Multi-axial experiments

---

Test	$\sigma_1$ [MPa]	$\sigma_2$ [MPa]	$\sigma_3$ [MPa]	$p$ [MPa]	$q$ [MPa]	$\theta^\circ$
TT1	88.14	46.85	10	48.33	55.28	28.12

Table 4.1: Results of the true-triaxial experiment under plane-strain condition

- Axial and lateral displacement of the specimen
- Axial and transversal strain of the specimen
- Fluid pressure applied to the specimen, i.e.  $\sigma_3$
- Displacement of the linear bearing

It is noted that the test was axial displacement controlled using a displacement rate of  $0.0005 \text{ m s}^{-1}$ , which was monitored from the average of the two axial LVDTs measurements.

## 4.5 Results

For the purpose of this study, four experiments in the Plane-Strain Apparatus were performed: one true-triaxial test ran under plane strain condition, one axisymmetric triaxial compression test and two attempts of true-triaxial test under constant mean-stress.

### 4.5.1 True-triaxial experiment under plane strain condition

The true-triaxial experiment under plane strain condition was performed at with a minor stress (i.e.  $\sigma_3$ ) magnitude of 10 MPa. Table 4.1 summarize the results of the experiments by presenting the stress state achieved at failure of the specimen.

The stress-strain plot, presented in Figure 4.10, shows the evolution of the three principal stresses after the hydrostatic loading at 10 MPa. After reaching its peak value, the axial stress decreased rapidly which reveals the brittle post-peak behavior of the rock subject to this state of stress. By keeping  $\epsilon_2 = 0$  through the test (Figure 4.11), the intermediate stress increased linearly until the major stress reached its peak value. At this point, failure of the specimen is achieved and the strain  $\epsilon_2$  increase so does the intermediate stress. The minor stress was kept constant in accordance with the experiment requirements.

Figure 4.12 shows the failed specimen the plane exposed to the pistons that applied the intermediate stress, i.e. from the  $(\sigma_3 - \sigma_1)$  plane where the failure surface formed. The specimen presents a kink in the failure surface at the middle of the specimen, leading to two different angles ( $75^\circ$  and  $65^\circ$ ). This have also been observed in previous experiments performed in the plane strain apparatus [6]. At failure, the steeper rupture surface occurs and the ability to control the stress state is lost which create a dynamic process, leading to a less steep rupture surface.

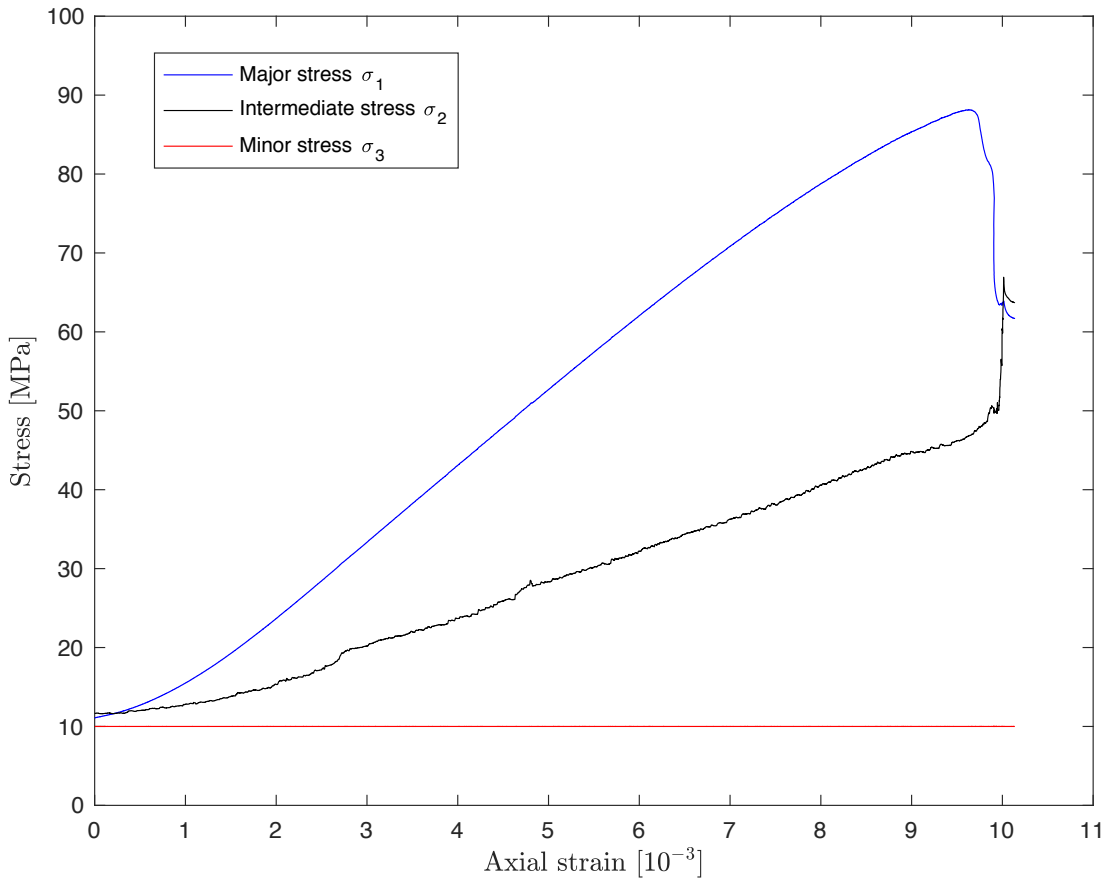


Figure 4.10:  $\sigma - \epsilon_a$  plot for the true-triaxial experiment performed under plane strain condition

Test	$\sigma_1$ [MPa]	$\sigma_2$ [MPa]	$\sigma_3$ [MPa]	$p$ [MPa]	$q$ [MPa]	$\theta^\circ$
TT 2	99.95	20	20	46.65	62.28	0

Table 4.2: Results of the axisymmetric triaxial experiment on a prismatic specimen

#### 4.5.2 Axisymmetric triaxial compression experiment on a prismatic specimen

The axisymmetric triaxial compression test was performed at a confining stress (i.e.  $\sigma_2 = \sigma_3$ ) of 20 MPa. This minor stress was chosen to be close to the highest value allowed by the pressure cell capacity, which was 24 MPa. Table 4.2 summarize the results of the experiments by presenting the stress state at achieved at failure of the specimen.

The stress-strain plot, presented in Figure 4.13, shows the evolution of the three principal stresses after the hydrostatic loading at 20 MPa. After the axial stress reached a peak value of 99.95 MPa, it started to decrease before stabilizing around 95 MPa. This post-peak tendency of the axial stress can be explained by the dilatancy of the specimen along the failure surface after it was formed, and the use of axial displacement control during the experiment. The minor and intermediate stresses were kept constant in accordance with the experiment conditions

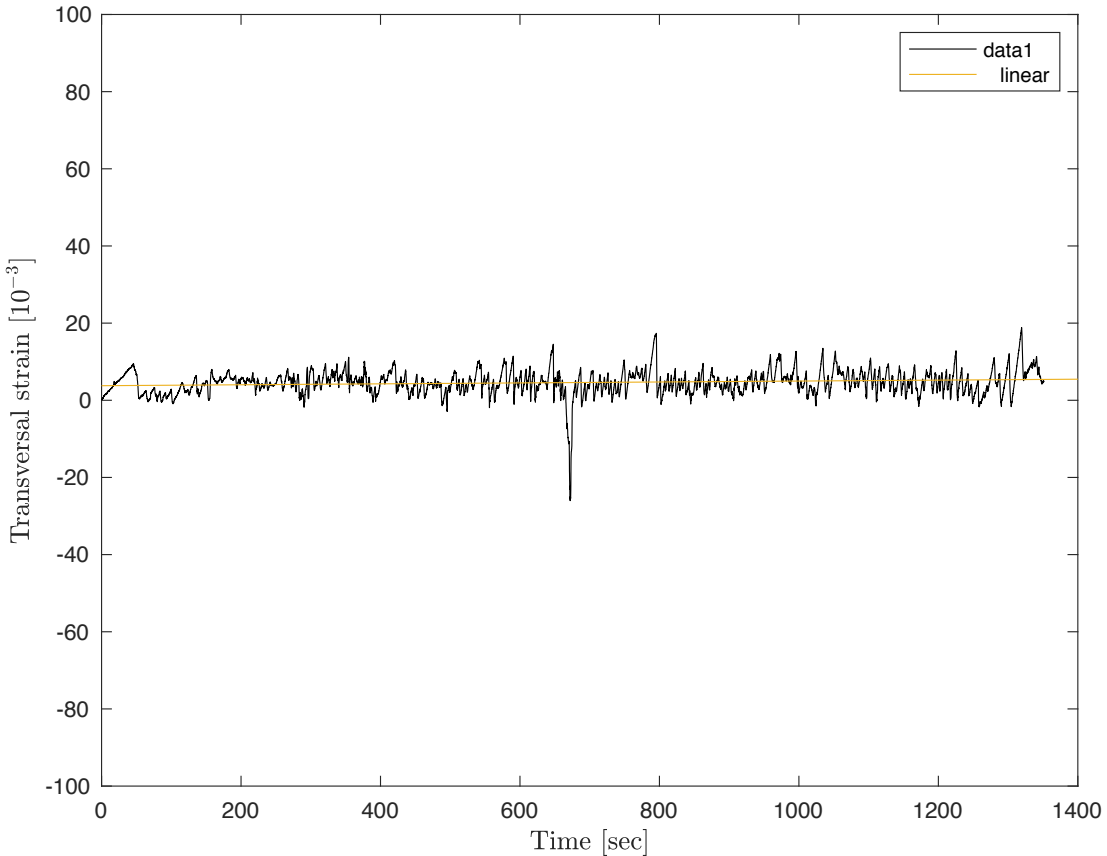


Figure 4.11:  $\epsilon$  - time plot for true-triaxial experiment under plane strain condition

Test	$\sigma_1$ [MPa]	$\sigma_2$ [MPa]	$\sigma_3$ [MPa]	$p$ [MPa]	$q$ [MPa]	$\theta^\circ$
TT 2	99.95	20	20	46.65	62.28	0
CTC 5	91.08	20	20	44.72	71.08	0

Table 4.3: Results of the true-triaxial experiment under plane-strain condition

requirements.

Figure 4.14 shows the failed specimen a) from the side perpendicular to the minor stress direction, and b) from the bottom (perpendicular to the axial stress). It presents a failure surface oriented at  $66^\circ$  in the  $(\sigma_I - \sigma_{II})$  directional plane, starting from the top right and ending at the bottom middle of the specimen.

A comparison with the conventional triaxial compression test performed at 20 MPa is presented in Table 4.3. It shows a difference of  $\sim 10\%$  of axial stress at peak, the higher being reached by the prismatic specimen in the Plane-Strain Apparatus.



Figure 4.12: Failure surface of the TT 1 specimen

#### 4.5.3 True-triaxial experiment under constant mean stress condition

Two unsuccessful attempts to perform a true-triaxial test under constant mean stress condition were made for this study. This test results were supposed to be compared with the one of the true-triaxial test performed under plane strain condition. Therefore, the stress path followed for the test presented in this section was based on the mean stress reach at failure for TT1.

figure 4.15 schematically represents the procedure defined in section 4.4. The initial phase is a hydrostatic loading to achieve 10 MPa, which correspond to the minor stress applied in the first experiment. Starting from the second phase to the end, the minor stress is kept at 10 MPa. At the end of the second phase (i.e. “deviatoric” loading phase 2), the mean stress that would be kept constant until the end of the test, is achieved. For this test, the magnitude of the major and intermediate stresses at the end of this phase were back calculated from the mean stress at failure of the first test, following Equations 4.7 to 4.10.

$$p_{TT1} = 48.3 \text{ MPa} \quad \text{and} \quad \sigma_3 = 10 \text{ MPa} \quad (4.7)$$

$$\sigma_{1,\text{init}} = \sigma_{2,\text{init}} = \sigma_{1,2} \quad (4.8)$$

$$p_{\text{initial}} = \frac{2\sigma_{1,2} - \sigma_3}{2} = 48.3 \text{ MPa} \quad (4.9)$$

$$\sigma_{1,2,\text{int}} = \frac{3p_{\text{initial}} - \sigma_3}{2} = 67.5 \text{ MPa} \quad (4.10)$$

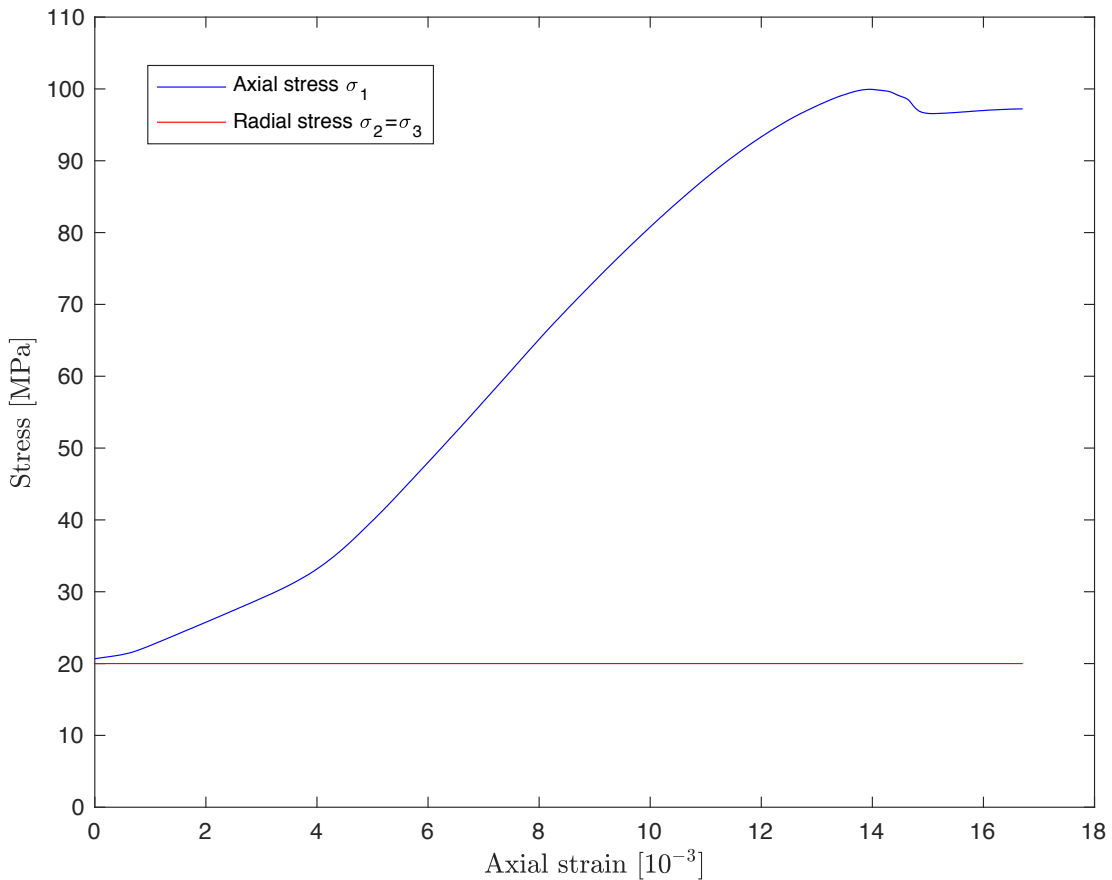


Figure 4.13:  $\sigma - \epsilon_a$  plot for the axisymmetric triaxial compression experiment

The two attempts to perform this test were stopped during this second phase. Indeed, as the major and intermediate stresses were increased at the same rate to  $\sigma_{1,2} = 67 \text{ MPa}$ ,  $\sigma_2$  dropped the first time before reaching 60 MPa and the second time before 25 MPa. In the first attempt, one of the pistons came out its housing with the O-ring exposed and broken. Moreover, the specimen did not show external signs of failure, leading to the conclusion that the intermediate stress dropped because of a leak from the pistons. Once the pistons fixed, a second attempt was made with the same result, and the hypothesis of leaking pistons was excluded. The specimen extracted from its polyurethane coat showed a rupture plane in the  $(\sigma_2 - \sigma_3)$  directional plane (Figure 4.16) leading to the following conclusions:

- The specimen failed during the first attempt
- Failure occurred when  $\sigma_2 > \sigma_1$  and  $\sigma_2$  became the major stress

The failure of the specimen prove that the state path applied to the specimen was not appropriate for the rock. In order to verify this assumption, the predicted axial stress at failure for the conditions of the test ( $\sigma_3 = 10 \text{ MPa}$  and  $\sigma_2 = 60 \text{ MPa}$ ) was computed using the three-parameter Paul-Mohr-Coulomb failure criterion. The theoretical background of the criterion

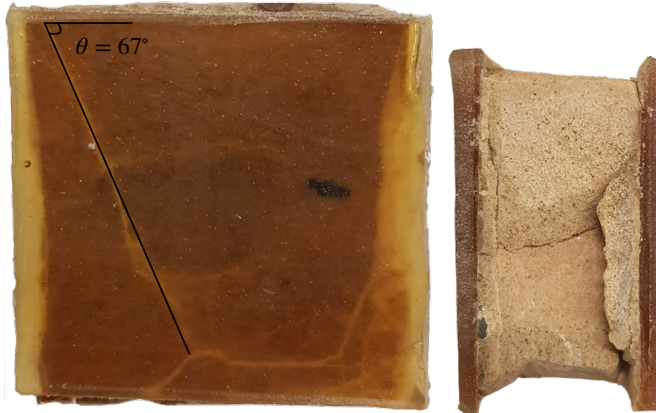


Figure 4.14: Failure surface of the TT2 specimen from the side and bottom

Table 4.4: Results of the true-triaxial experiment under plane-strain condition

$\sigma_1$ [MPa]	$\sigma_2$ [MPa]	$\sigma_3$ [MPa]
59	60.0	10.0

is detailed in Chapter 3 and its strength parameters obtained for Dunnville sandstone are presented in Chapter 5. The predicted  $\sigma_1$  at failure is presented in Table 4.4. The state of stress at failure obtained is very close to the one applied to the specimen during the test before it failed, and, therefore, was not appropriate for this experiment. Moreover, it is in agreement with the directional change of the major stress revealed by the orientation of the failure plane. To conclude, the compatibility between the foreseen experiment stress state and the rock strength should have been checked before performing the experiment.

This experiment also showed that the constant mean stress procedure cannot be applied based on the state of stress reached at failure for the plane strain experiment. Nonetheless, it would be interesting to modify the constant mean stress procedure by choosing to add a condition on the deviatoric stress  $q$  or on the Lode angle  $\theta$ .

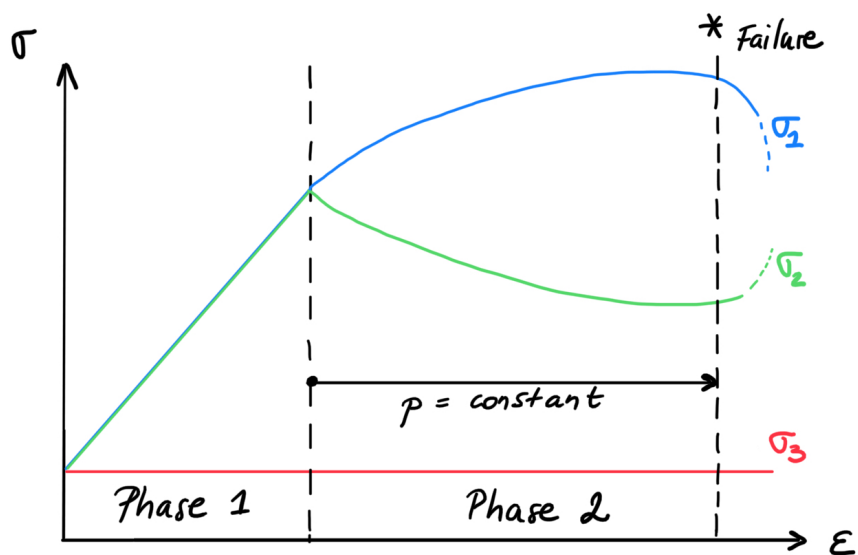


Figure 4.15: Sketch of the procedure for true-triaxial experiment under constant mean stress condition



Figure 4.16: Failure surface on constant mean stress test specimen

# 5 Results analysis and Discussion

## 5.1 Overview

The main objective of this study was evaluate of three failure criteria for a selected rock, Dunnville sandstone. As explained in the previous chapters, the empirical nature of most failure criteria requires a thick database of diverse multi-axial experiments for their development.

Dunnville sandstone have been used for several works in the past and particularly for multi-axial experiments [1][3][2]. The tests performed in the scope of this study (cf. Chapter 4) presented the opportunity to enrich the existing database and to evaluate the failure criteria with data representative of Dunnville sandstone response.

The database presented in Table 5.1 is based on the work of Zeng et al. (2019) [3] and extended with the results of the experiments from this study. In this table, each experiment is associated with the following elements: the orientation of the bedding regarding the application of the axial stress, the three principal stresses  $\sigma_I, \sigma_{II}, \sigma_{III}$  and the stress invariants ( $p, q, \theta$ ). This database was used for the evaluation of Mohr-Coulomb, Hoek-Brown and Paul-Mohr-Coulomb failure criteria.

## 5.2 Evaluation of the failure criteria

The Mohr-Coulomb, Hoek-Brown and Paul-Mohr-Coulomb failure criteria presented in Chapter 2 were fitted to the experiment results of Dunnville sandstone from Table 5.1. A computation program was developed for the fittings using the programming language Python. All the resources needed to access the program files are listed in Appendix REFAPPENDIX B.

The three failure criteria are evaluated through their representation in the three coordinates systems presented in Chapter 2, and their accuracy in terms of how good they fit the data. In this study, this "accuracy" is chosen to be evaluated by comparing the least mean standard deviation misfits, as proposed by Benz et al. (2008) [16].

## Chapter 5. Results analysis and Discussion

---

Table 5.1: Database of experiments results for Dunnville Sandstone. The "Published" data are from Zeng et al. (2019) [3]

Test	Bedding	$\sigma_I$ [MPa]	$\sigma_{II}$ [MPa]	$\sigma_{III}$ [MPa]	$p$ [MPa]	$q$ [MPa]	$\theta$ [°]
Published TC-1	⊥	29.7	0.0	0.0	9.9	29.7	0
Published TC-2	⊥	39.4	2.5	2.5	14.8	36.9	0
Published TC-3	⊥	52.9	5.0	5.0	21.0	47.9	0
Published TC-4	⊥	71.5	10.0	10.0	30.5	61.5	0
Published TC-5	⊥	98.4	20.0	20.0	46.1	78.4	0
Published TC-6	⊥	114.5	30.0	30.0	58.2	84.5	0
Published TC-7	⊥	129.4	40.0	40.0	69.8	89.4	0
Published TC-8	⊥	142.1	50.0	50.0	80.7	92.1	0
Published TC-9	⊥	153.8	60.0	60.0	91.3	93.8	0
Published TC-10		24.9	0.0	0.0	8.3	24.9	0
Published TC-11		35.2	2.5	2.5	13.4	32.7	0
Published TC-12		48.8	5.0	5.0	19.6	43.8	0
Published TC-13		68.0	10.0	10.0	29.3	58.0	0
Published TC-14		95.9	20.0	20.0	45.3	75.9	0
Published TC-15		110.9	30.0	30.0	57.0	80.9	0
Published TC-16		125.5	40.0	40.0	68.5	85.5	0
Published TC-17		138.1	50.0	50.0	79.4	88.1	0
Published TC-18		150.8	60.0	60.0	90.3	90.8	0
UCS	⊥	29.8	0	0	27.95	51.43	0
TC 9	⊥	49.43	5	5	19.81	44.43	0
TC 0	⊥	61.43	10	10	27.95	51.43	0
TC 5	⊥	91.08	20	20	44.72	71.08	0
TC 8	⊥	127.3	40	40	65.73	87.30	0
TC 10	⊥	151.1	60	60	88.12	91.10	0
Published TE-1	⊥	35.0	35.0	0.8	23.6	34.2	60
Published TE-2	⊥	40.0	40.0	1.2	27.1	38.8	60
Published TE-3	⊥	50.0	50.0	6.0	35.3	44.0	60
Published TE-4	⊥	60.0	60.0	10.1	43.4	49.9	60
Published TE-5	⊥	69.0	69.0	11.5	49.8	57.5	60
Published TE-6		40.0	40.0	1.8	27.3	38.2	60
Published TE-7		50.0	50.0	5.7	35.2	44.3	60
Published TE-8		60.0	60.0	8.0	42.7	52.0	60
TE 3	⊥	35	35	3.96	24.64	31.08	60
TE 1	⊥	40	40	4.50	27.89	36.34	60
TE 2	⊥	60	60	9.68	43.01	50.98	60
Published TT-1	⊥	48.3	31.6	5.0	28.3	37.8	37.5
Published TT-2	⊥	52.9	25.1	7.0	28.3	40.1	22.7
Published TT-3	⊥	63.9	12.1	9.0	28.3	53.4	2.9
Published TT-4	⊥	70.6	49.4	15.0	45.0	48.7	37.8
Published TT-5	⊥	77.5	70.5	20.0	56.0	54.3	53.5
Published TT-6	⊥	83.9	62.1	22.0	56.0	54.4	39.7
TT 1	⊥	88.14	46.85	10	48.33	55.28	28.12
TT 2	⊥	99.98	20	20	46.65	62.28	0

The standard deviation  $s_i$  of one test series  $i$  formed by  $j$  experiments subject to the same minor stress ( $\sigma_{III}$ ) is defined by Equation 5.1. In this expression,  $n$  is the number of experiments in the test series  $i$ ,  $\sigma_{I,j}^{\text{test}}$  is the maximum stress at failure for a data point  $j$  (obtained from the database) and  $\sigma_{I,j}^{\text{calc}}$  is the calculated one using the considered criterion formulation.

$$s_i = \sqrt{\frac{1}{n} \sum_j (\sigma_{I,j}^{\text{calc}} - \sigma_{I,j}^{\text{test}})^2} \quad (5.1)$$

Finally, the mean standard deviation misfit is computed following Equation 5.2, where  $m$  is the number of test series. The smaller the  $\bar{S}$  is, the better is the prediction of the model for the rock compared to other criteria. A criterion that would perfectly fit the data will present no misfits.

$$\bar{S} = \frac{1}{m} \sum_i s_i \quad (5.2)$$

### 5.2.1 Mohr-Coulomb failure criterion

The Mohr-Coulomb failure criterion is formulated in terms two principal stresses (Equations 2.17 and 2.18) and unique strength parameters ( $\phi, c$ ), therefore, the fitting was done using only axisymmetric triaxial compression tests results ( $\theta = 0^\circ$ ).

From this fitting, the coefficients  $K_p$  and  $C_0$  were determined and the other parameters were computed:

$$K_p = 2.026 \quad \text{and} \quad C_0 = 41.78 \text{ MPa} \quad (5.3)$$

$$\phi = \frac{K_p - 1}{K_p + 1} = 19.43^\circ \quad (5.4)$$

$$c = \frac{C_0(1 - \sin\phi)}{2\cos\phi} = 14.79 \text{ MPa} \quad (5.5)$$

$$V_0 = \frac{C_0}{K_p - 1} = 40.73 \text{ MPa} \quad (5.6)$$

Knowing the strength parameters, the Mohr-Coulomb failure surface is plotted in the  $(\sigma_3 - \sigma_1)$  plane using Equation 2.17(Figure 5.1).

The criterion was also fitted in the  $(p - q)$  plane, for which the plot obtained is shown in Figure 5.2. The coefficients  $m_{c,e}$  and  $b_{c,e}$  were computed using Equations 2.33 to 2.36:

$$m_c = \frac{6 \sin \phi}{3 - \sin \phi} = 0.76 \quad (5.7)$$

$$m_e = \frac{6\sin\phi}{3 + \sin\phi} = 0.61 \quad (5.8)$$

$$b_c = \frac{6c\cos\phi}{3 - \sin\phi} = 31.1 \text{ MPa} \quad (5.9)$$

$$b_e = \frac{6c\cos\phi}{3 + \sin\phi} = 24.8 \text{ MPa} \quad (5.10)$$

Finally, the Mohr-Coulomb criterion is presented in the  $\pi$ -plane, obtained following the procedure described in Section 2.2.1. Figure 5.3 shows Mohr-Coulomb failure criterion in the  $\pi$ -plane at different values of the mean stress  $p$ .

The mean standard deviation misfit obtained with the Mohr-Coulomb failure criterion is 17.7 MPa.

### 5.2.2 Hoek-Brown failure criterion

The Hoek-Brown failure criterion is also formulated in terms two principal stresses (Equations 2.37) and strength parameters ( $m$ ,  $C_0$ ). Therefore, the fitting was done using only axisymmetric triaxial compression tests results ( $\theta = 0^\circ$ ).

From this fitting, the strength parameters  $m$  and  $C_0$  was determined and  $V_0$  was computed:

$$m = 3.10 \quad \text{and} \quad C_0 = 42.35 \text{ MPa} \quad (5.11)$$

$$V_0 = \frac{C_0}{m} = 13.65 \text{ MPa} \quad (5.12)$$

Knowing the strength parameters, the Hoek-Brown failure surface is plotted in the  $(\sigma_3 - \sigma_1)$  plane using Equations 2.38 for the compression line and 2.39 for extension (Figure 5.1).

In the  $(p - q)$  plane, the Hoek-Brown failure criterion is plotted using Equations 2.42 for compression and 2.43 for extension, and shown in Figure 5.5. These surfaces are expressed in terms of  $m$  and  $C_0$  previously defined.

Finally, the Hoek-Brown criterion is presented in the  $\pi$ -plane, obtained following the procedure described in Section 2.2.2. Figure 5.6 shows Hoek-Brown failure criterion in the pi-plane at different values of the mean stress  $p$ .

The mean standard deviation misfit obtained with the Hoek-Brown failure criterion is 17.5 MPa.

## 5.2. Evaluation of the failure criteria

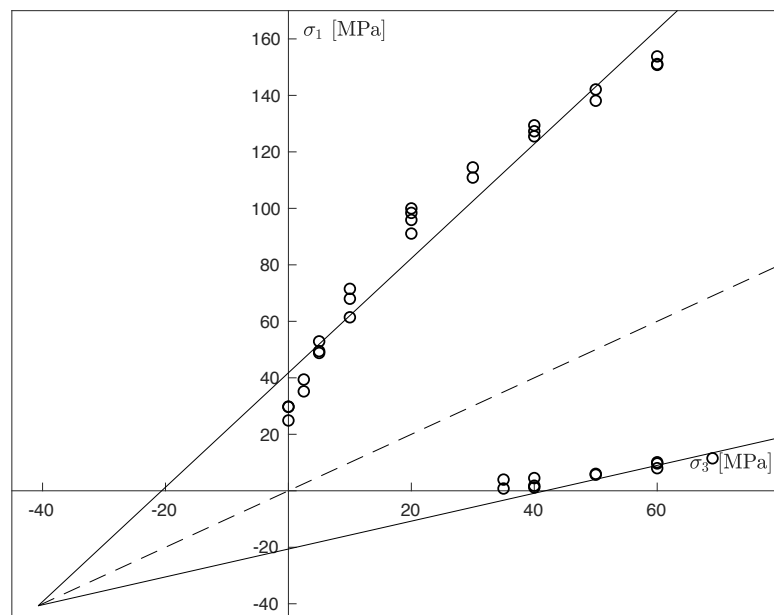


Figure 5.1: Mohr-Coulomb criterion failure surface in  $(\sigma_3 - \sigma_1)$  plane

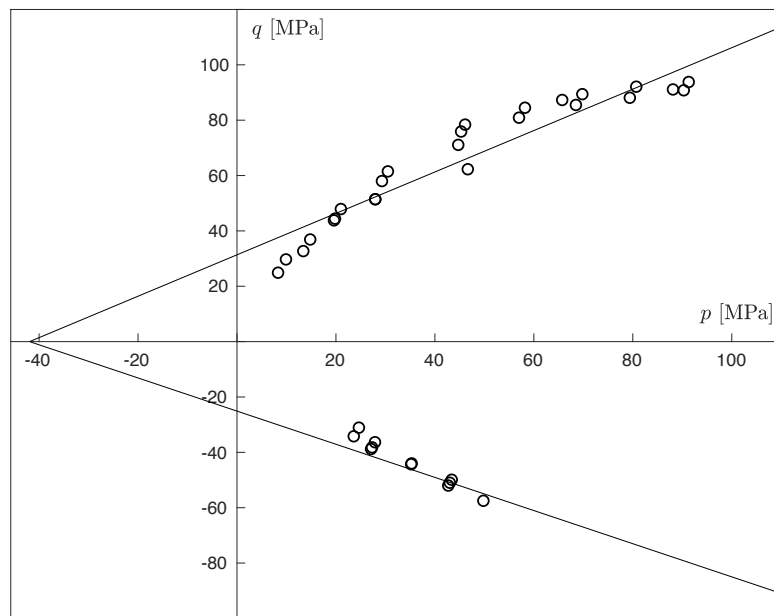
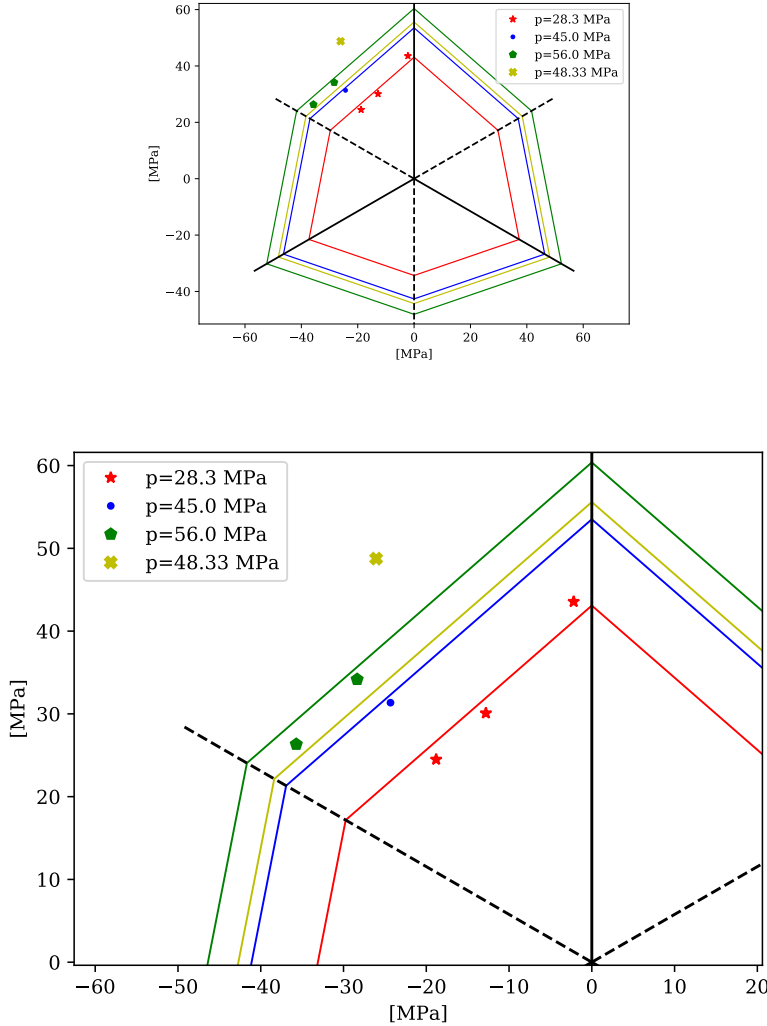


Figure 5.2: Mohr-Coulomb criterion failure surface in  $(p - q)$  plane


 Figure 5.3: Mohr-Coulomb criterion failure surface in  $\pi$ -plane

### 5.2.3 Paul-Mohr-Coulomb failure criterion with one plane

Contrary to the previous criteria, the Paul-Mohr-Coulomb failure criterion is formulated in terms the three principal stresses (Equations 2.44 and 2.48) and non-unique strength parameters (i.e.  $\phi_{c,e}$ ,  $c_{c,e}$ ,  $V_0$ ). Therefore, the fitting was done using all tests results from the database.

From the least-square solution fitting described in Chapter 2 (cf. Section 2.3, Equations 2.57 and 2.62), the following solution could be obtained:

$$x_1 = \frac{b_c}{V_0} = 0.81 \quad (5.13)$$

## 5.2. Evaluation of the failure criteria

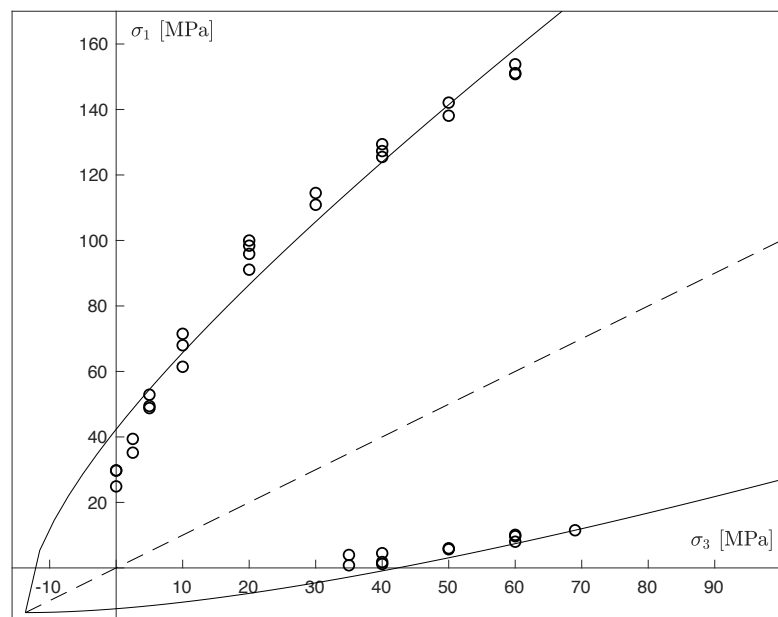


Figure 5.4: Hoek-Brown criterion failure surface in  $(\sigma_3 - \sigma_1)$  plane

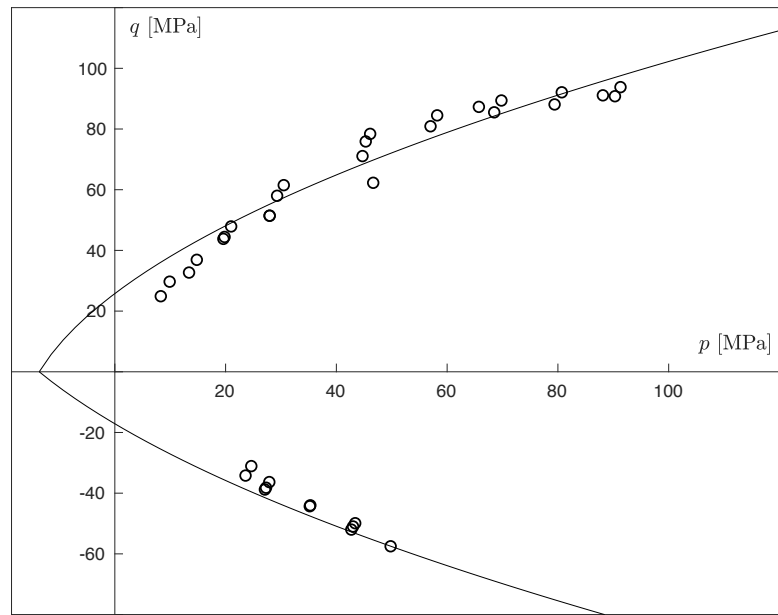


Figure 5.5: Hoek-Brown criterion failure surface in  $(p - q)$  plane

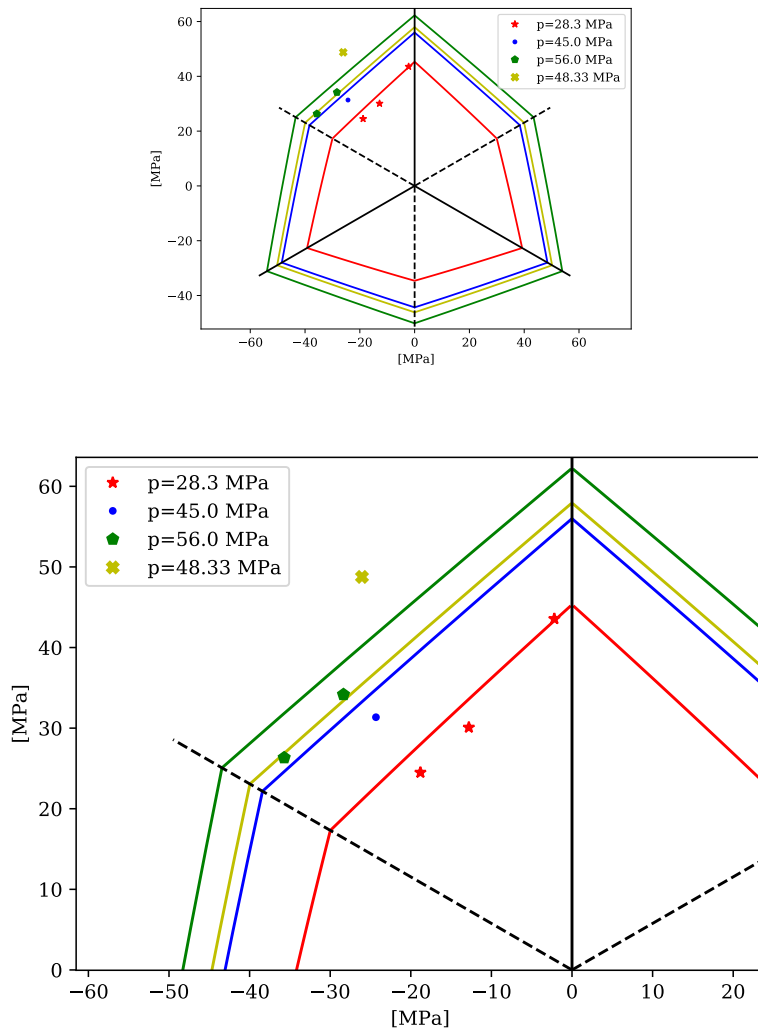


Figure 5.6: Hoek-Brown criterion failure surface in  $\pi$ -plane

$$x_2 = k = -0.91 \quad (5.14)$$

$$x_3 = b_c = 28.77 \text{ MPa} \quad (5.15)$$

Following Equations 2.61 to 2.65, the strength parameters for Paul-Mohr-Coulomb failure criteria can be computed:

$$V_0 = \frac{0.81}{b_c} = 35.62 \text{ MPa} \quad (5.16)$$

$$b_e = \frac{2b_c}{(1 - \sqrt{3}k)} = 22.31 \text{ MPa} \quad (5.17)$$

$$\phi_c = \arcsin\left(\frac{3b_c}{6V_0 + b_c}\right) = 20.85^\circ \quad (5.18)$$

$$\phi_e = \arcsin\left(\frac{3b_e}{6V_0 - b_c}\right) = 20.46^\circ \quad (5.19)$$

$$c_c = \frac{b_c(3 - \sin\phi_c)}{6\cos\phi_c} = 13.57 \text{ MPa} \quad (5.20)$$

$$c_e = \frac{b_e(3 + \sin\phi_e)}{6\cos\phi_e} = 10.52 \text{ MPa} \quad (5.21)$$

Knowing the strength parameters, the Paul-Mohr-Coulomb failure surface can be plotted in the  $(\sigma_3 - \sigma_1)$  plane using Equations 2.49 to 2.51. The graph obtained, using the coefficients computed in Equations 5.22 to 5.25, is presented in Figure 5.7.

$$M_c = \frac{1 + \sin\phi_c}{1 - \sin\phi_c} = 2.11 \quad (5.22)$$

$$M_e = \frac{1 + \sin\phi_e}{1 - \sin\phi_e} = 2.08 \quad (5.23)$$

$$C_c = \frac{2c_c \cos\phi_c}{1 - \sin\phi_c} = 39.38 \text{ MPa} \quad (5.24)$$

$$C_e = \frac{2c_e \cos\phi_e}{1 - \sin\phi_e} = 30.31 \text{ MPa} \quad (5.25)$$

In the  $(p - q)$  plane, the Paul-Mohr-Coulomb failure criterion is plotted using Equations 2.54 to 2.56, and the graph obtained in presented in Figure 5.8. These surfaces are expressed in terms of  $b_{c,e}$ , defined by Equations 5.15 and 5.17, and  $m_{c,e}$  computes as follow:

$$m_c = \frac{6\sin\phi_c}{3 - \sin\phi_c} = 0.81 \quad (5.26)$$

$$m_e = \frac{6\sin\phi_e}{3 + \sin\phi_e} = 0.63 \quad (5.27)$$

Finally, the Paul-Mohr-Coulomb criterion is presented in the  $\pi$ -plane, obtained following the procedure described in Section 2.2.3. Figure 5.9 shows the failure criterion in the  $\pi$ -plane at different mean stresses  $p$ , corresponding to true-triaxial experiments mean stresses at failure (i.e. data points where  $0^\circ < \theta < 60^\circ$  in Table 5.1).

## Chapter 5. Results analysis and Discussion

---

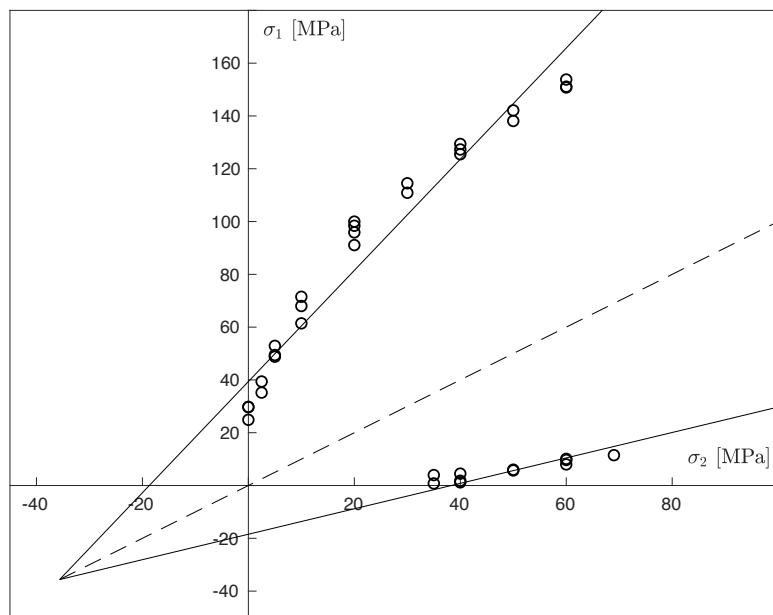


Figure 5.7: Paul-Mohr-Coulomb criterion failure surface in  $(\sigma_3 - \sigma_1)$  plane

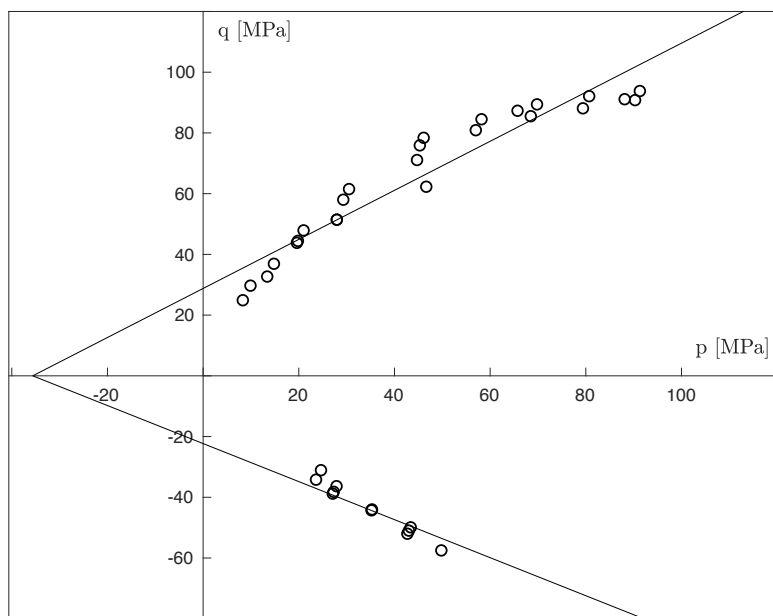
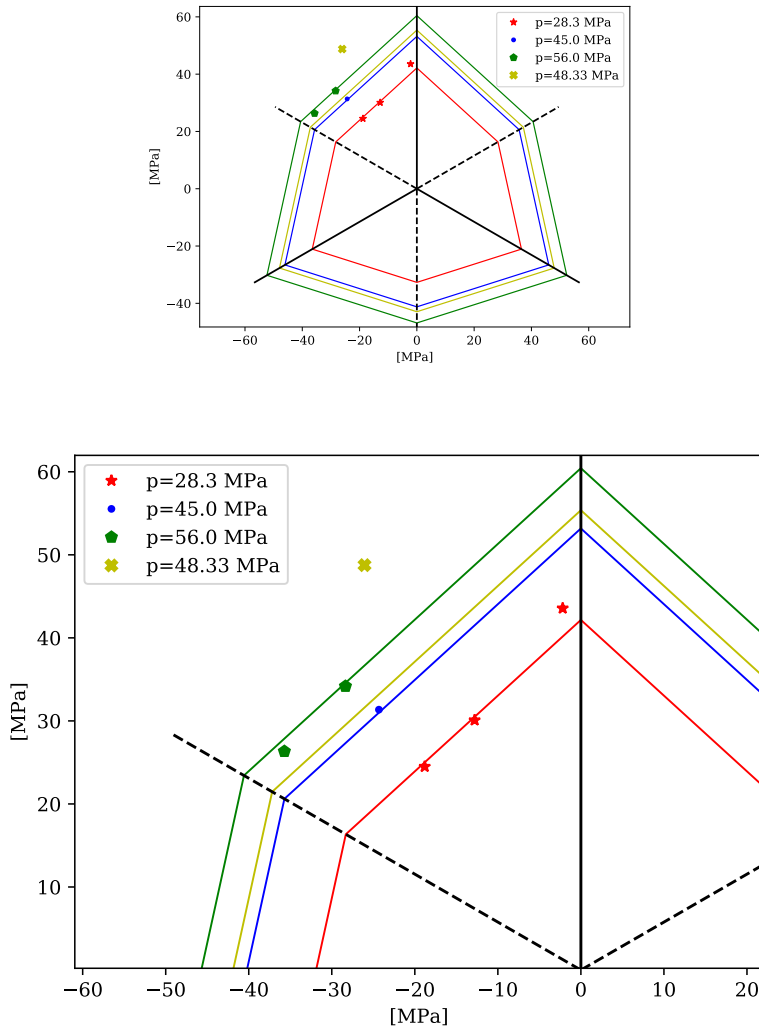


Figure 5.8: Paul-Mohr-Coulomb criterion failure surface in  $(p - q)$  plane


 Figure 5.9: Paul-Mohr-Coulomb criterion failure surface in  $\pi$ -plane

The mean standard deviation misfit obtained with the Paul-Mohr-Coulomb failure criterion is 16.7 MPa.

#### 5.2.4 Comparison of the failure criteria

The mean standard deviation misfits obtained for the three failure criteria show that Paul-Mohr-Coulomb provides a better approximation of the data points (Table 5.2). The three misfits values are very close and the observation of the fittings in the  $(\sigma_3 - \sigma_1)$  and  $(p - q)$  planes shows that the failure criteria provide similar approximations of the data points. However, in the  $\pi$ -plane the Paul-Mohr-Coulomb provide a better fitting of the true-triaxial data (Figure 5.9).

Table 5.2: Summary of the mean standard deviation misfits obtained for the three failure criteria evaluated

Criterion	Mean standard deviation misfit $\bar{S}$ [MPa]
Mohr-Coulomb	17.7
Hoek-Brown	17.5
Paul-Mohr-Coulomb, 1 plane	16.7

### 5.3 Paul-Mohr-Coulomb failure criterion with two planes

Published data from multi-axial experiments on multiple rocks showed that the failure envelop that describe them best is not linear over a large range of mean stress. However, popular failure theories as Mohr-Coulomb or Hoek-Brown, are either linear or do not provide an accurate prediction for all mean stresses. In this study, Paul-Mohr-Coulomb failure criteria is chosen to address this issue by approximating the nonlinear failure surface in a piecewise linear manner, resulting in a failure surface defined by six parameters.

#### 5.3.1 Paul-Mohr-Coulomb with six parameters

The Paul-Mohr-Coulomb failure criterion presented in the Section 5.2.3 is referred to as Paul-Mohr-Coulomb with three parameters and the failure surface is a plane defined by the general equation of the criterion (Equation 2.48) using  $V_0$ ,  $\phi_c$  and  $\phi_e$ . The Paul-Mohr-Coulomb failure surface defined in a piecewise manner is, therefore, made of a minimum of two planes, each expressed using three strength parameters, leading to the six parameters criterion.

The three parameter criterion describes a regular 6-sided pyramid in the principal stresses space (Section 2.1). By adding a plane to the failure surface, the six parameters criterion, therefore, describes two irregular 6-sided pyramids. Each plane is then defined by the parameters presented in Table 5.3, where  $P2$  indicates the plane that approximate data points at low mean stress and  $P1$  the ones at higher mean stress. Table 5.4 present four types of Paul-Mohr-Coulomb failure surfaces that can be defined according to the values of the parameters. For all types, the following conditions apply:

$$V_0^{(1)} > V_0^{(2)} \quad \text{and} \quad 0^\circ \leq \phi_{c,e}^{(i)} \leq 90^\circ \quad (5.28)$$

The complete graphical representation of the Paul-Mohr-Coulomb failure surface is composed of the  $(p - q)$  plane, the  $(\sigma_{II} - \sigma_I)$  plane, the  $\pi$ -plane and the principal stresses three-dimensional space. The transition between  $P2$  and  $P1$  is well represented in the  $(p - q)$  plane, where they intersect on the compression side at the mean stress value  $p_c$  and on the extension side at  $p_e$ . In the case of the failure surface type (ii), these transitions points have different values leading to a 12 sided transition zone on the pyramid for mean stress values  $p \in [p_c; p_e]$ . Sketches of the 6-12-6 sided failure surface in different planes and in the three-dimensional

### 5.3. Paul-Mohr-Coulomb failure criterion with two planes

Table 5.3: Parameters of the planes defining the failure surface of Paul-Mohr-Coulomb criterion

Plane	P1	P2
Friction angle in compression	$\phi_c^{(1)}$	$\phi_c^{(2)}$
Friction angle in extension	$\phi_e^{(1)}$	$\phi_e^{(2)}$
Theoretical uniaxial tensile strength	$V_0^{(1)}$	$V_0^{(2)}$

Type of failure surface	Parameters conditions
(i) 6-sided	$V_0^{(1)} = V_0^{(2)}$
(ii) 6-12-6 sided	$\phi_c^{(1)} < \phi_c^{(2)}, \phi_e^{(1)} < \phi_e^{(2)}, p_c \neq p_e$
(iii) 6-12 sided	$(\phi_c^{(1)} < \phi_c^{(2)}, \phi_e^{(1)} \geq \phi_e^{(2)})$ or $(\phi_c^{(1)} \geq \phi_c^{(2)}, \phi_e^{(1)} < \phi_e^{(2)})$
(iv) 6-12-6 sided	$\phi_c^{(1)} < \phi_c^{(2)}, \phi_e^{(1)} < \phi_e^{(2)}, p_c = p_e$

Table 5.4: Types of failure surfaces for the six parameters Paul-Mohr-Coulomb criterion

space are presented in Figure 5.10, where the  $(\sqrt{3}p - \sigma_1^*)$  plane is equivalent to the  $(p - q)$  plane. More schematic representations and details on the four failure surfaces types are provided in APPENDIX C REFAPPENDIX C.

The inclusion of the intermediate stress in the Paul-Mohr-Coulomb equation (Equation 2.44) makes relevant the representation of the criterion in the  $(\sigma_2 - \sigma_1)$  plane. Indeed, this plane presents the advantage to gather the data points for axisymmetric experiments, shown on compression and extension lines, as well as true-triaxial data in the same plot (Figure 5.11). The Paul-Mohr-Coulomb failure surfaces are plotted for a chosen value of  $\sigma_3$ , using the following equation, based the rearrangement of Equation 2.44:

$$\sigma_I = \frac{1}{A} (1 - B\sigma_{II} - C\sigma_{III}) \quad (5.29)$$

#### 5.3.2 2-planes fitting

The fitting of a six-parameter Paul-Mohr-Coulomb failure surface requires datasets for each plane. Once determined, these datasets are used for plane fitting, following the procedure presented in Section 2.3. This repartition of the data points into different planes is a challenging step of the failure criterion fitting, as it should give the optimal solution for the database considered.

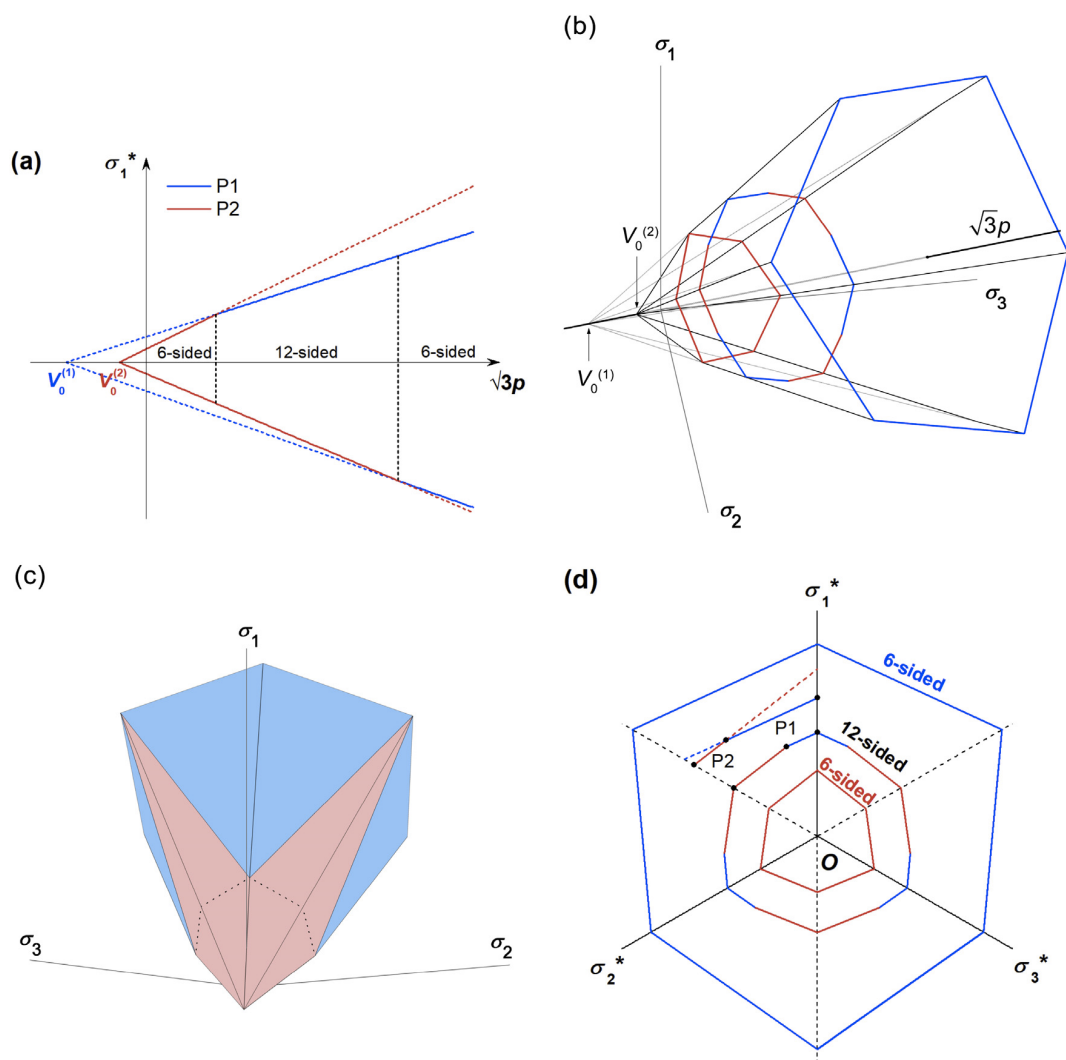


Figure 5.10: Paul-Mohr-Coulomb 6-12-6 sided failure surface graphical representations

### 5.3. Paul-Mohr-Coulomb failure criterion with two planes

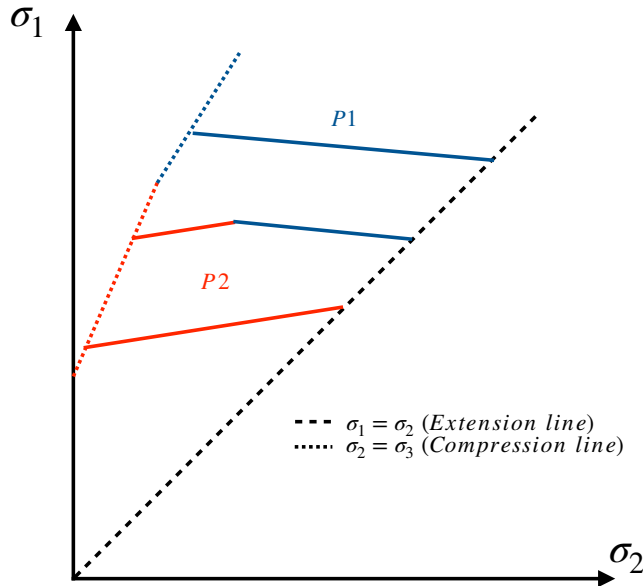


Figure 5.11: Paul-Mohr-Coulomb 6-12-6 sided failure surface in  $(\sigma_{II} - \sigma_I)$  plane

One objective of this study was to create a program that automatically allocates data points to both planes, with the aim of getting a distribution that provides the best fitting for the Paul-Mohr-Coulomb criterion. Moreover, it was crucial that this program was developed not only for the rock tested in this study (i.e. Dunnville Sandstone), but for any rock with appropriate experimental data. This problem can be summarized by the following question:

*How to automatize the allocation of data points into  $P1$  or  $P2$  in order to provide the most accurate fitting of the Paul-Mohr-Coulomb criterion ?*

In the following paragraphs, the algorithm created to solve this problem is described.

#### Algorithm construction

The algorithm developed to solve the problem presented belongs to the *Brute-force* algorithm family. This category is based on the following principle: every possibility offered by the database is tried and the one that gives the best solution to the problem is selected. The amount of data available in the case of rock testing ( $n_{max} \sim 50$ ) is small enough to use this type of algorithm without having issues related to efficiency.

In the case of this study, the algorithm will test all the possible variations of data allocations to the  $P1$  or  $P2$  datasets which can be created from the rock database. For each possible combination, planes  $P1$  and  $P2$  are created by the computation of their coefficient and fitting parameters defined for Paul-Mohr-Coulomb, following the procedure presented in 2.3. Then, the Mean Square Error ( $MSE$ ), defined by Equation 5.31, is computed for each combination

## Chapter 5. Results analysis and Discussion

---

of datasets. Finally the data allocation variation that provides the minimal  $MSE$  is selected as the solution of the two planes fitting problem.

The algorithm proposed in this study can be apply to any rock testing database that contains results of the three principal stresses at failure (Table 5.1). Indeed, the rock database is the only input that is required to run this algorithm.

### Computation of the mean square error

The error used in the computation of  $MSE$  is equal to the distance of a data point, defined by  $\sigma_I$ ,  $\sigma_{II}$  and  $\sigma_{III}$ , from its fitted plane, defined by Equation 2.44:

$$err_i = A^{(j)}\sigma_I^i + B^{(j)}\sigma_{II}^i + C^{(j)}\sigma_{III}^i - 1 \quad (5.30)$$

where  $i$  is the index of the data point in the database and  $j$  indicates the plane number in which the data is allocated (i.e.  $j = 1$  for  $P1$  and  $j = 2$  for  $P2$ ). The Mean Square Error of a certain dataset combination  $k$  is then computed as follow:

$$MSE_k = \frac{1}{n} \sum_{i=1}^n err_i^2 \quad (5.31)$$

The dataset combination  $k$  that obtains the minimal  $MSE$  value provides the best fitting solution for Paul-Mohr-Coulomb failure surface for the considered rock.

### Program resources

This algorithm was implemented in the programming language Python. The resources on the program developed to solve the two planes fitting problem are gathered in APPENDIX B. It contains the Python files required to run the program and a *README* document that explains how to use the program. Moreover, all the code files are commented in detail to ease their use and understanding.

#### 5.3.3 Dunnville sandstone

The program presented in the previous section was applied to the experimental results database of Dunnville sandstone (cf. Table 5.1). The six parameters Paul-Mohr-Coulomb failure surface obtained is presented in the following paragraphs through its representation in the  $(p - q)$ ,  $(\sigma_{II} - \sigma_I)$ ,  $\pi$ - planes and in the principal stresses three-dimensional space.

### Strength parameters computation

The solution obtained from the least-square solution fitting describe in Chapter 2 (cf. Section 2.3, Equations 2.57 and 2.62) is presented in Table 5.5.

### 5.3. Paul-Mohr-Coulomb failure criterion with two planes

---

The strength parameters for Paul-Mohr-Coulomb failure criteria could be computed from Equations 2.61 to 2.65. The values obtained are gathered in Table 5.6.

#### Graphical representation of the failure surface

Knowing the strength parameters, the Paul-Mohr-Coulomb failure surface could be plotted in the  $(p - q)$  plane using Equations 2.54 to 2.56 applied to each plane. The values of parameters  $m_{c,e}$  and  $c_{c,e}$  are presented in Table 5.7 and the  $(p - q)$  plane plot is shown in Figure 5.12.

The failure surface can also be plotted in the  $(\sigma_{II} - \sigma_I)$  plane. Equation 5.29 provides the planes equation in this coordinates system using the general expression of the Paul-Mohr-Coulomb criterion, which coefficients  $A$ ,  $B$  and  $C$  are presented in Table 5.8. Figure 5.13 presents the six parameters failure surface for Dunnville sandstone in the  $(\sigma_{II} - \sigma_I)$  plane.

The failure surface planes are also presented in the  $\pi$ -plane, obtained following the procedure described in Section 2.2.3. Figure 5.14 shows the failure criterion in the  $\pi$ -plane at different mean stresses  $p$  that correspond to true-triaxial experiments mean stresses at failure for  $0^\circ < \theta < 60^\circ$  in Table 5.1. In addition, Figure 5.15 presents the projection of the  $P_2, P_2 - P_1$  transition and  $P_1$  pyramids on the  $\pi$ -plane.

Finally, Figure 5.16 shows the 6-12-6 sided pyramid obtained for Dunnville sandstone in the three-dimensional space.

A summary of the Paul-Mohr-Coulomb six parameters solution and the mean standard deviation misfits obtained for Dunnville Sandstone is presented in Table 5.9. The fittings provided by Mohr-Coulomb, Hoek-Brown, three and six parameters Paul-Mohr-Coulomb criteria can be compared using the mean standard deviation misfits values obtained (Table 5.2). The six parameter Paul-Mohr-Coulomb criterion provides the best prediction with the least mean standard deviation misfits for the two planes. This can be explained by the combination of the intermediate stress inclusion in the failure criterion general equation and the approximation of the failure surface non linearity, giving the most accurate states of stress prediction at failure. The observation of the six parameter Paul-Mohr-Coulomb and Hoek-Brown fittings in the  $(p - q)$  and  $\pi$ - planes also presents for the first one a better approximation of the true-triaxial data points, but also of the axisymmetric ones, which was not the case with the three parameter Paul-Mohr-Coulomb.

The program developed for the Paul-Mohr-Coulomb criterion was generalized so that it can be used to fit of other rocks. A summary of the results obtained for rocks with available database from literature is provided in APPENDIX D REFAPPENDIX D.

## Chapter 5. Results analysis and Discussion

---

Plane	$x_1^{(i)}$	$x_2^{(i)}$	$x_3^{(i)}$
$P1$	0.54	-1.02	47.08
$P2$	1.39	-1.10	15.47

Table 5.5:  $P1$  and  $P2$  least-square solutions  $x$  for Dunnville sandstone

Plane	$b_c^{(i)}$ [MPa]	$b_e^{(i)}$ [MPa]	$V_0^{(i)}$ [MPa]	$\phi_c^{(i)}$ [ $^\circ$ ]	$\phi_e^{(i)}$ [ $^\circ$ ]
$P1$	47.1	34.1	86.9	14.4	12.1
$P2$	15.5	10.7	11.1	34.3	34.8

Table 5.6:  $P1$  and  $P2$  strength parameters for Dunnville sandstone

Plane	$m_c^{(i)}$ [-]	$m_e^{(i)}$ [-]	$c_c^{(i)}$ [MPa]	$c_e^{(i)}$ [MPa]
$P1$	0.54	0.39	22.3	16.2
$P2$	1.39	0.96	7.61	5.26

Table 5.7:  $P1$  and  $P2$  fitting parameters for Dunnville sandstone

Plane	$A^{(i)}$	$B^{(i)}$	$C^{(i)}$
$P1$	$1.74 \times 10^{-2}$	$4.26 \times 10^{-3}$	$-3.32 \times 10^{-2}$
$P2$	$3.47 \times 10^{-2}$	$-8.31 \times 10^{-4}$	$-1.24 \times 10^{-1}$

Table 5.8: Paul-Mohr-Coulomb general equation coefficients for Dunnville sandstone

Plane	$V_0^{(i)}$ [MPa]	$\phi_c^{(i)}$ [ $^\circ$ ]	$\phi_e^{(i)}$ [ $^\circ$ ]	$\bar{S}$ [MPa]
$P1$	86.9	14.4	12.1	14.9
$P2$	11.1	34.3	34.8	6.12

Table 5.9: Summary of  $P1$  and  $P2$  strength parameters for Dunnville sandstone

### 5.3. Paul-Mohr-Coulomb failure criterion with two planes

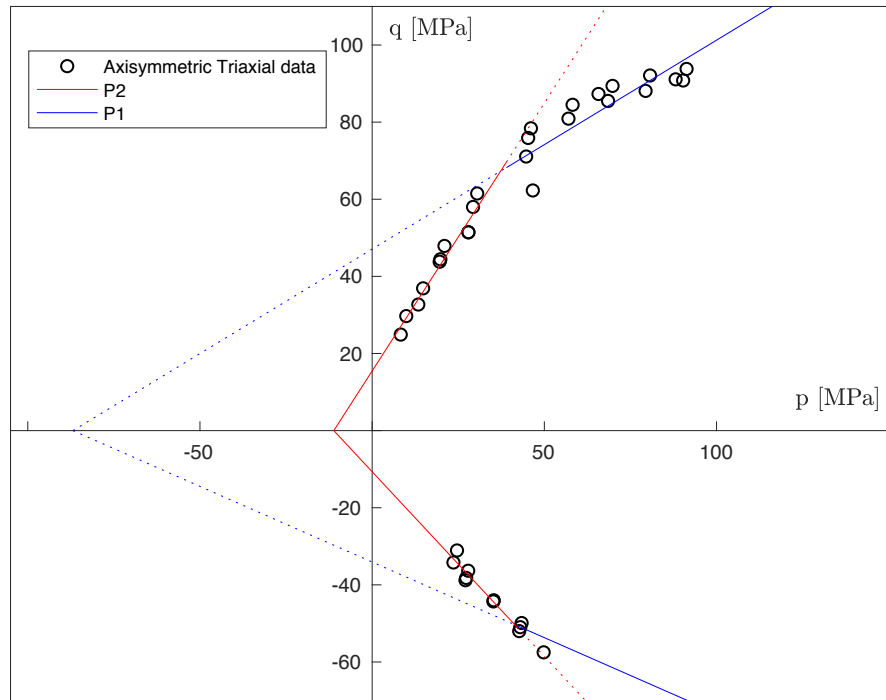


Figure 5.12: Paul-Mohr-Coulomb failure surface in the  $(p - q)$  plane for Dunnville sandstone

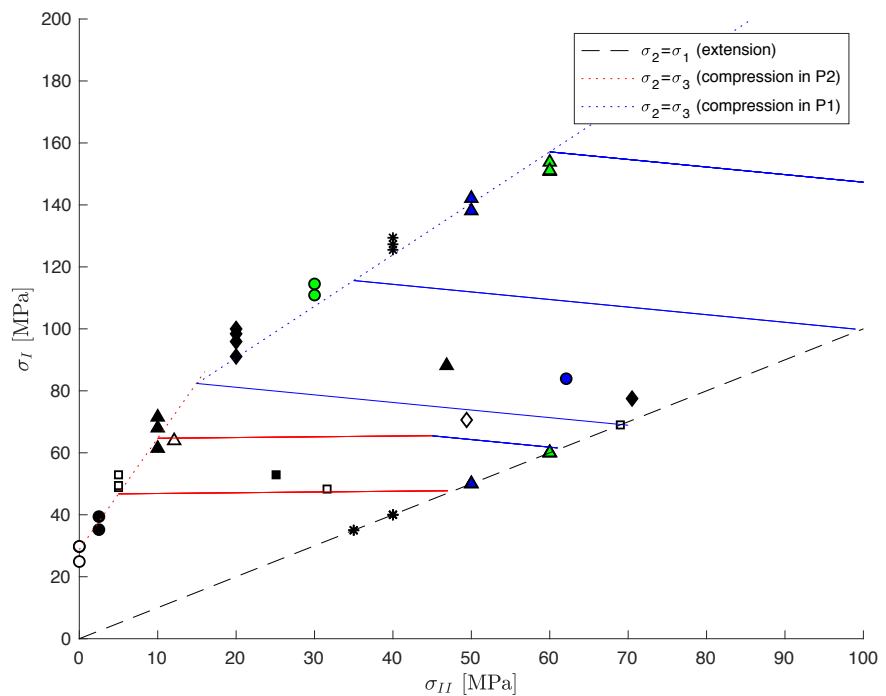


Figure 5.13: Paul-Mohr-Coulomb failure surface in the  $(\sigma_{II} - \sigma_I)$  plane for Dunnville sandstone

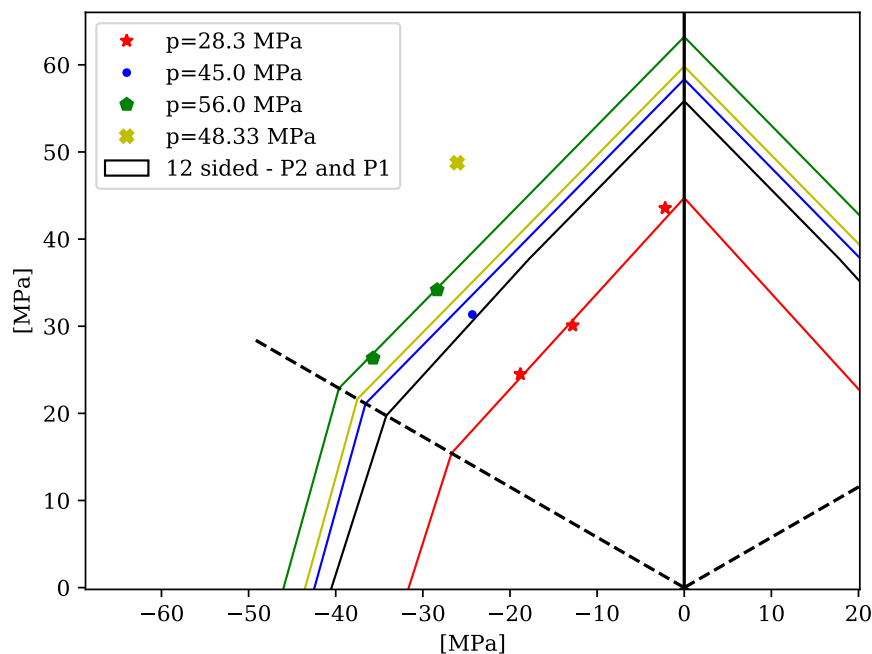


Figure 5.14: Paul-Mohr-Coulomb failure surface in the  $\pi$ -plane for Dunnville sandstone

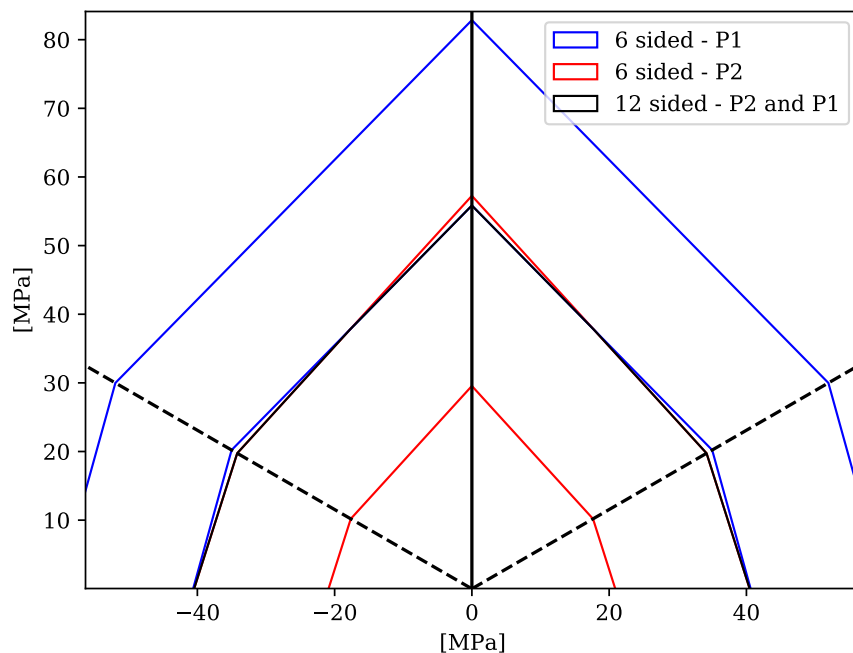


Figure 5.15: 6-12-6 sided pyramid projection in the  $\pi$ -plane for Dunnville sandstone

### 5.3. Paul-Mohr-Coulomb failure criterion with two planes

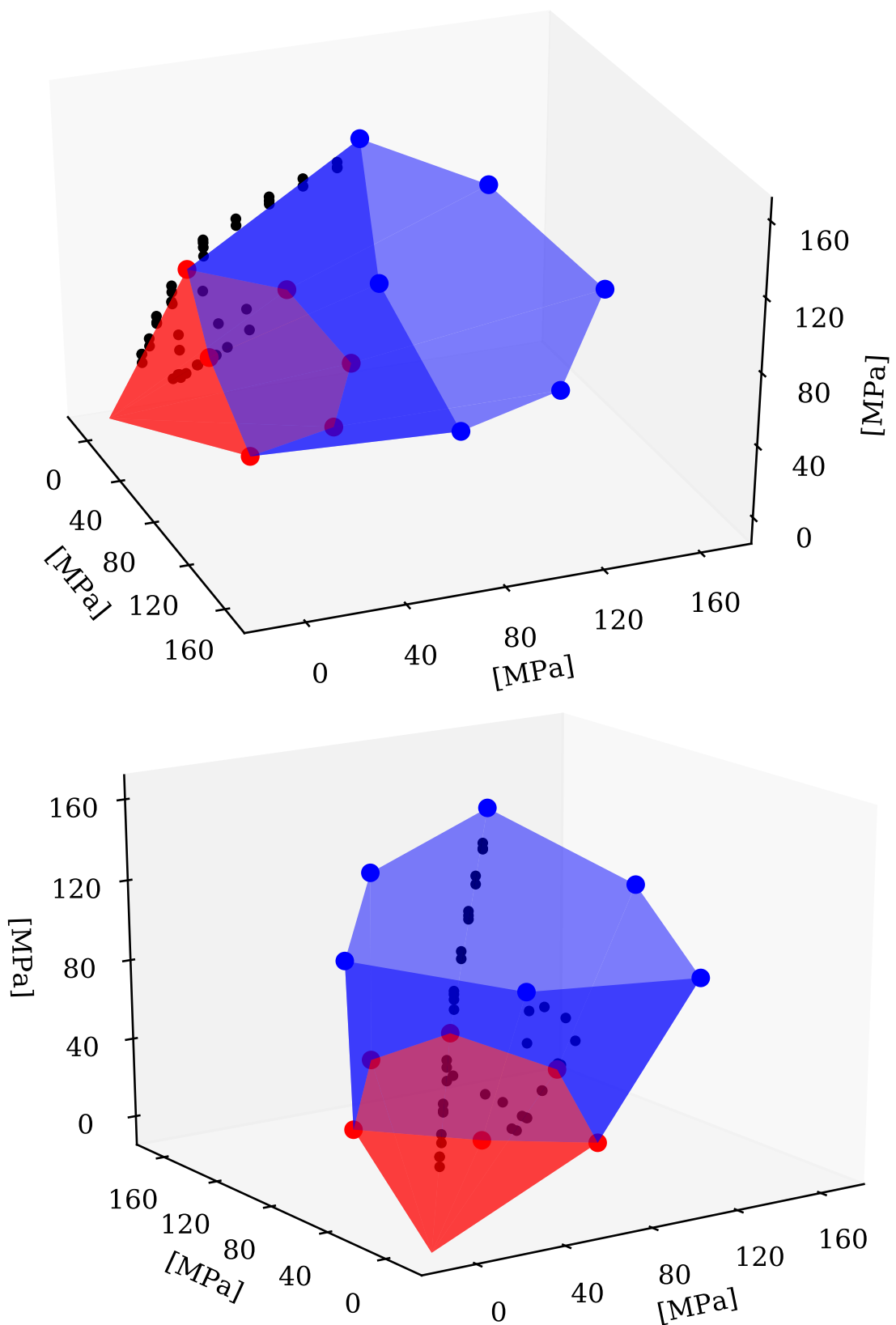


Figure 5.16: Paul-Mohr-Coulomb 6-12-6 sided failure surface pyramid for Dunnville sandstone

## 5.4 Discussion

The previous sections provide a comparison of the four failure criteria principally based on the computation of the mean standard deviation misfits  $\bar{S}$ . This quantitative comparison indicator is based on the computation of the error between the predicted and real values of the major stress, and report the precision of the prediction provided by a failure criterion. Another comparison could also be relative to the failure surface. Indeed, a rigorous evaluation of a failure criterion can be made by the computation of the distance between a data point and the failure surface. This type of error computation was used in this work in the *Brute-force* algorithm developed for the six parameters Paul-Mohr-Coulomb fitting (Section 5.3.2). In this case, as well as for Mohr-Coulomb, the computation of the "point-plane" distance is made possible and convenient thanks to the explicit general equation of the planes that forms the failure surface. However, in the case of Hoek-Brown and other criteria defined by implicit equations, it becomes challenging to go through the mathematical derivations required to compute this distance. An interesting addition to this work would be to look at all the criteria evaluated here from the point of view of the "data-failure surface" distance, and to compare the quantitative indicators of their accuracy.

On the  $\pi$ -plane representations of the failure criteria (Figure 5.14) the data point of the true-triaxial experiment under plane strain condition (i.e.  $p = 48.3$  MPa) presents an outlier from the failure surface but also from the "alignment" or "group" of other true-triaxial data (mainly performed under constant mean stress). The experiments from previous work ("Published" data in Table 5.1) were performed on specimens from a different block than the one used for the tests presented in this study. Therefore, it is possible that the specimen used for the plane strain test had different strength properties, leading to this outlier. This unique true-triaxial data point for plane strain testing stresses out the need for a more detailed investigation on true-triaxial experiments performed under various state of stress. However, it should be noted that performing this type of experiment is challenging and time consuming, which makes difficult to gather data for the same rock.

The comparison of the three failure criteria revealed the importance of taking into account the intermediate stress in their formulation. First, the evaluation of the Mohr-Coulomb and Paul-Mohr-Coulomb indicates that even with the use of a linear criterion to approximate a non-linear failure surface, the one defined by a general equation in terms of the three principal stresses gives a better approximation of the data points. Moreover, the comparison between the Hoek-Brown and Paul-Mohr-Coulomb fittings reveals that a linear criterion that takes into account  $\sigma_{II}$  gives a better fitting of the data from true-triaxial experiments, which is more representative of in-situ conditions.

The work presented in this study showed that the six parameter Paul-Mohr-Coulomb failure criterion provides the most accurate approximation of the failure surface as well as a good prediction of the state of stress at failure compared to Mohr-Coulomb and Hoek-Brown. Nonetheless, one criticism can be addressed to this criterion regarding the amount of ex-

periments required to construct the two plane failure surface. Indeed, in order to build the failure surface of the three parameters Paul-Mohr-Coulomb criterion, three data points are needed, leading to a requirement of six points for the six parameters criterion. These six data points corresponds to the same number of experiments, ideally of different procedures, that is needed to be performed on the same rock. By carrying out this study in an well equipped research environment, it was possible to perform multiple experiments under different conditions. However, this is hardly the case in the majority of rock mechanics and geoengineering applications for which that amount of data is not always available. From this point of view, Mohr-Coulomb and Hoek-Brown are more convenient to apply to a small amount of data, which is why they are popular and widely use.

\*\*\*\*\* 4 parameter PMC \*\*\*\*\* Say that Paul-Mohr-Coulomb is better  
\*\*\*\*\*



# 6 Conclusion

## 6.1 Conclusion

The purpose of this study was to evaluate the Mohr-Coulomb, Hoek-Brown and Paul-Mohr-Coulomb failure criteria by analyzing the results of multi-axial experiments performed on Dunnville sandstone.

First, a review the three failure criteria was provided, where they were presented thought the definition of their material parameters in different coordinates systems. The strength parameters used the criteria formulations are the frictions angles in compression  $\phi_c$  and in extension  $\phi_e$ , the theoretical isotropic tensile strength  $V_0$ , the uniaxial compressive strength  $C_0$  and the fitting parameter  $m$ . The parameters for the Mohr-Coulomb and Hoek-Brown failure criteria computation was based on the results of axisymmetric triaxial experiments, as they do not include the intermediate stress  $\sigma_{II}$  in their definition. The three parameter Paul-Mohr-Coulomb failure criteria is defined by the three principal stresses, and its parameters were computed with the results of all multi-axial data, using a fitting method based on the least squares solution. Other parameters were defined to represent the failure criteria in the  $(p - q)$ ,  $(\sigma_3 - \sigma_1)$  and  $\pi$ - planes.

Dunnville sandstone was presented though its geological history and mineralogy, and its behavior under uniaxial and multi-axial testing was observed by performing a uniaxial compression test and several conventional (axisymmetric) triaxial experiments. In order to investigate the intermediate stress effect on rock failure, four true-triaxial experiments under different stress paths were performed using the University of Minnesota Plane-Strain Apparatus. The addition of pistons enabling the direct application of the intermediate stress ( $\sigma_{II}$ ) gave the possibility to perform a true-triaxial experiment with a plane strain testing condition ( $\epsilon_2 = 0$ ).

The results of the experiments performed in the scope of this study enriched the available data from multi-axial experiments on Dunnville sandstone, and were gathered with results published in literature in a database. This database was then used to evaluate the Mohr-Coulomb, Hoek-Brown and three parameter Paul-Mohr-Coulomb failure criteria. Their comparison,

based on the least mean standard deviation misfits, showed that the three parameter Paul-Mohr-Coulomb provided the best prediction and fitting of the experimental data, thanks to the inclusion of the intermediate stress and the definition of different frictions angles for compression and extension.

The Paul-Mohr-Coulomb failure criterion was further investigated by evaluating its accuracy using a failure surface described by two planes instead of one, leading to a six parameter Paul-Mohr-Coulomb failure criterion. The failure criterion fitting was enabled by the development of a program, in the coding environment Python, that automatically allocated the data to the failure surface plane that minimize the mean squared error of the distance between the two-plane failure surface and the data points. This program was generalized to enable its use for all rocks with available results of multi-axial experiments.

The evaluation of the three failure criteria for Dunnville sandstone showed that Paul-Mohr-Coulomb provide the most accurate prediction and fitting of the failure surface, whether it is made of one plane or two planes.

## 6.2 Future work

As the evaluation of the failure criteria is based on the multi-axial experiments results, the improvement and extension of rock databases is crucial. Future work on this subject could be to continue the investigation of the intermediate stress effect, by performing other true-triaxial experiments with plane strain condition and to diversify the testing conditions. An interesting modification of the experiments presented in this thesis could be to perform true-triaxial tests with a constant Lode angle condition instead of a mean stress one. This could be a way to investigate the effect of the Lode angle value on failure of rocks.

# Bibliography

- [1] J. F. Labuz, F. Zeng, R. Makhnenko, and Y. Li, "Brittle failure of rock: A review and general linear criterion," *Journal of Structural Geology*, vol. 112, pp. 7–28, jul 2018. doi: 10.1016/j.jsg.2018.04.007
- [2] A. Tarokh, "Poro-elastic response of saturated rock." phdthesis, Department of Civil, Environmental and Geo-Engineering, University of Minnesota, 2016, p.71.
- [3] F. Zeng, B. L. Folta, and J. F. Labuz, "Strength testing of sandstone under multi-axial stress states," *Geotechnical and Geological Engineering*, vol. 37, no. 6, pp. 4803–4814, may 2019. doi: 10.1007/s10706-019-00939-5
- [4] C. J. Jaeger and N. G. W. Cook, *Fundamentals of Rock Mechanics, 3rd edition.* Chapman and Hall, 1979.
- [5] E. Hoek, E. T. Brown, and E. Vol, "Empirical strength criterion for rock masses," *Journal of the Geotechnical Engineering Division, ASCE.*, vol. 106, pp. 1013–1015, 1980.
- [6] J. Labuz, S.-T. Dai, and E. Papamichos, "Plane-strain compression of rock-like materials," *International Journal of Rock Mechanics and Mining Sciences & Geomechanics Abstracts*, vol. 33, no. 6, pp. 573–584, sep 1996. doi: 10.1016/0148-9062(96)00012-5
- [7] R. Makhnenko and J. Labuz, "Plane strain testing with passive restraint," *Rock Mechanics and Rock Engineering*, vol. 47, no. 6, pp. 2021–2029, nov 2013. doi: 10.1007/s00603-013-0508-2
- [8] B. Paul, "Generalized pyramidal fracture and yield criteria," *International Journal of Solids and Structures*, vol. 4, pp. 175–196, 1968.
- [9] J. P. Meyer and J. F. Labuz, "Linear failure criteria with three principal stresses," *International Journal of Rock Mechanics and Mining Sciences*, vol. 60, pp. 180–187, jun 2013. doi: 10.1016/j.ijrmms.2012.12.040
- [10] B. Folta, "Strength testing under multi-axial stress states," Master's thesis, Department of Civil, Environmental and Geo-Engineering, University of Minnesota, 2016. [Online]. Available: <http://hdl.handle.net/11299/182131>

## Bibliography

---

- [11] M. Ostrom, “Cambrian stratigraphy in western wisconsin,” 1966. [Online]. Available: [https://wgnhs.wisc.edu/pubs/download\\_ic07/](https://wgnhs.wisc.edu/pubs/download_ic07/)
- [12] R. Ulusay, “The isrm suggested methods for rock characterization, testing and monitoring: 2007-2014,” *ISRM*, 2015.
- [13] “Practices for preparing rock core as cylindrical test specimens and verifying conformance to dimensional and shape tolerances,” 2019. doi: 10.1520/d4543-19
- [14] J. Labuz and J. Bridell, “Reducing frictional constraint in compression testing through lubrication,” *International Journal of Rock Mechanics and Mining Sciences & Geomechanics Abstracts*, vol. 30, no. 4, pp. 451–455, aug 1993. doi: 10.1016/0148-9062(93)91726-y
- [15] J. Franklin and E. Hoek, “Developments in triaxial testing technique,” *Rock mechanics*, vol. 2 (4), p. 223–228.
- [16] T. Benz and R. Schwab, “A quantitative comparison of six rock failure criteria,” *International Journal of Rock Mechanics and Mining Sciences*, vol. 45, no. 7, pp. 1176–1186, oct 2008. doi: <https://doi.org/10.1016/j.ijrmms.2008.01.007>